Collaborative project

Project acronym: SNM

Project full title: "**Single Nanometer Manufacturing for beyond CMOS devices**"

Grant agreement no: 318804

Deliverable: D1.10 ("Parallel closed loop lithography operation with 4 cantilever system demonstrated")

Name of the coordinating person: Prof. Dr. Ivo W. Rangelow, Email: ivo.rangelow@tu-ilmenau.de

List of participants:

Participant no.	Participant organisation name	Part. short name	Activity Type	Country
1 (Co)	Technische Universität Ilmenau	**TUIL**	HER	Germany
2	EV Group E. Thallner GmbH	**EVG**	IND; End-user	Austria
3	IMEC	**IMEC**	RES	Belgium
4	Mikrosistemi Ltd	**µS**	SME; End-User	Bulgaria
5	Universität Bayreuth	**UBT**	HER	Germany
6	Technische Universiteit Delft	**TUD**	HER	Netherlands
7	Spanish National Research Council	**CSIC**	RES	Spain
8	IBM Research GmbH	**IBM**	IND; End-user	Switzerland
9	École polytechnique fédérale de Lausanne	**EPFL**	HER	Switzerland
10	SwissLitho AG	**SL**	SME; End-User	Switzerland
11	Oxford Instruments Nanotechnology Tools Ltd	**OINT**	IND; End-user	UK
12	Imperial College London	**IMPERIAL**	HER	UK
13	The Open University	**OU**	HER	UK
14	Oxford Scientific Consultants Ltd	**OSC**	SME	UK
15	VSL Dutch Metrology Institute	**VSL**	IND	Netherlands
16	University of Liverpool	**ULIV**	HER	UK

SNM **Work Package 1** **Deliverable: D1.10 ("Parallel closed loop lithography operation with 4 cantilever system demonstrated")**										
Lead beneficiary number	1	**Nature**	R	**Dissemination level**	PU					
Estimated Person-months	40									
Person-months by partner for the Deliverable	TUIL									
	38.22									
Estimated Delivery Date	M48: 12/2016	**Delivery Date**	04/2017							
Author	• Ivo W. Rangelow, Marcus Kaestner, Claudia Lenk, Nikolay Nikolov, Ahmad Ahmad, Tihomir Angelov									
Reviewed by:	• WP1 Leader: Marcus Kaestner • WPG1 Leader: Armin Knoll • Coordinator: Ivo W. Rangelow									
Criteria and Achieved Results	**Criteria**	**Achieved result**								
	a) Design, fabrication and assembly FE-SPL technology platform integrating a four ("Quattro") cantilever arrays.	Achieved. A full overlap of single working fields is enabled. A mechanical tilt correction is introduced. Electronics and software previously developed are fully integrated allowing 4 cantilever operation in parallel manner.								
	b) Demonstration of parallel imaging (AFM) capability.	Achieved. Simultaneous imaging using all four cantilever of a "Quattro" cantilever array was demonstrated. Imaging of a 0.5x0.2 mm scan area was achieved with an								

		effective scanning speed of 5.6 mm/s.
	c) Demonstration of parallel lithography (FE-SPL) capability.	Partially achieved. Field emissions scanning probe lithography (FE-SPL) was demonstrated with two out of four cantilever of a “Quattro” cantilever array.
Description of the Deliverable	**Executive Summary** In frame of the SNM project throughput enhancement of tip-based nanofabrication should be demonstrated by employing cantilever arrays. In this context, the simultaneous operation of <n>-cantilever increases the throughput by n-times. In order to exploit the full capability of scanning probe based nanolithography a closed loop lithography for all cantilever of an array was targeted. In this context, the parallel operation capability of both (1) imaging in AFM mode as well as (2) lithography, so called field-emission scanning probe lithography (FE-SPL), has been developed. As defined in DoW, TUIL has planned to demonstrate the upscaling capability by simultaneous operation of four cantilever in parallel manner. The so called “Quattro” cantilever arrays are fabricated on the basis of a silicon-on-insulator (SOI) wafer using surface micromachining and gas chopping plasma-etching processes, described in detail in frame of deliverable report D1.8. Due to the integration of thermomechanical actuation and piezoresistive deflection read-out on each individual cantilever of the array, we are able to actuate and measure each cantilever independently. By implementation of advanced control routines, as shown later, the individual actuation in static (DC) and dynamic (AC) operation as well as their superposition (= AC oscillation at resonance frequency + quasi-static DC deflection working as individual Z-scanning unit) is enabled. Thus, each cantilever has integrated it’s own AC-actuation, DC-deflection as well as deflection read-out unit enabling an individual operation of each cantilever of an array system. In a first step TUIL and µS designed, fabricated and assembled a FE-SPL closed loop lithography technology platform, which is able to work with four cantilever simultaneously. Therefore, the hardware was designed, fabricated and assembled. A 200 x 200 x 20 µm	

[X/Y/Z] piezoscanning stage is integrated. Since the tip-to-tip distance between adjacent cantilever of an array is 125 µm a full overlap of single working fields is enabled. The Quattro-cantilever array chip, reported in D1.8, is mounted on a dedicated PCB holder. The contacts between cantilever chip and holder are bonded. The counterpart of the cantilever holder is directly attached to the XYZ piezoscanning unit. A high precision tilt correction mechanism was integrated. The system is capable to compensate errors of ±3° with a resolution of 0.25° between sample surface and Quattro cantilever array. The electronics (controller, analog frontend, etc.) as well as the four-cantilever software previously developed and described in deliverable report D1.5 was integrated and tested allowing 4 cantilever operation in parallel manner. In this context, several challenges and difficulties not considered during initial developments in frame of D1.5 were faced during implementation. These were solved but led to delays for final implementation (details are explained below). The implemented high throughput data transfer system for mask data handling and data transfer is explained in detail in deliverable report D1.9. In frame of the work crosstalk effects between neighboring cantilevers of an array are investigated and minimized.

In context of the deliverable the parallel AFM imaging capability using AC amplitude modulation (AM) was demonstrated. The employed actuation scheme is based on superposition of AC and DC thermomechanical actuation. Thereby, the AC part leads to an oscillation of the cantilever at resonance frequency, which is required for the AM-AFM feedback loop. The DC part is the quasi-static deflection of the cantilever at low frequencies, which is applied for tracking of the topography. The entire range of the static bending of the cantilever is used in order to adjust individually the working set-point as well as to track the surface topography. For imaging purpose relatively soft cantilever were applied (22 N/m), which gives an acceptable actuation efficiency with a total DC deflection range (peak-to-peak) of approx. 2-5 µm. The tilt compensation is applied in order adjust the array in parallel manner with respect to the sample surface. All remaining tip-sample distance variations, e.g. arising from remaining tilt after compensation, from differences in tip height and pre-deflection, are compensated by the DC thermomechanical actuation. In order to compensate the overall system drift caused by temperature drift, etc., which could be up to five-times larger than the Z-range of the cantilever, a second low bandwidth feedback loop

is integrated controlling the z-piezoscanner unit. Here, while Feedback-1 tracks the topography Feedback-2 determines the DC voltage set-point for Feedback-1 and keeps it constant. Thus, it is ensured that the sample surface is kept in range of the thermomechanical DC actuation range. As a result, simultaneous imaging using all four cantilever of a "Quattro" cantilever array was demonstrated. Imaging of a 0.5x0.2 mm scan area was achieved with an effective scanning speed of 5.6 mm/s. In addition, sub-nm resolution in vertical direction of each single cantilever was demonstrated. Here, a freshly cleaved highly oriented pyrolytic graphite (HOGP) surface was imaged simultaneously with 4 cantilever showing in each image single atomic steps. The results are published: Ahmad, A., Nikolov, N., Angelov, T., Ivanov, T., Reum, A., Atanasov, I., Guliyev, E., Ishchuk, V., Kaestner, M., Krivoshapkina, Y., Lenk, S., Lenk, C., Rangelow, I.W., Holz M., „Large area fast-AFM scanning with active "Quattro" cantilever arrays", Journal of Vacuum Science and Technology B 34, 06KM03 (2016).

In terms of lithographic applications the parallel operation of field emission scanning probe lithography (FE-SPL) was targeted. Therefore, the emission of each cantilever has to be controlled separately by integration of four independently working feedback loops. Thereby, the emission of each cantilever is separately measured via independent high-precision transimpedance and amplification (= IU-converter) units, which are placed close to the Quattro-cantilever chip. Thereby, the Quattro cantilever chip design (ref. D1.8) is based on a SOI substrate, which ensures an electronic separation during field-emission current measurement. In final state TUIL has demonstrated parallel FE-SPL with two out of four cantilever of a "Quattro" cantilever array. Here, the trade-off in cantilever requirements for imaging and lithography was underestimated. In particular, due to the electrostatic (=Coulomb) forces appearing during lithographic operation relative stiff (e.g. 90 N/m) cantilevers are required in order prevent feedback-loop instabilities (instabilities leads to jump-to-contact problems resulting in a tip-crash and shortcut). This was proven by experiment as well as simulations. As a drawback of stiff cantilever the actuation efficiency is reduced. This in turn leads to significantly decreased DC actuation ranges. In particular, the available actuation range of each single cantilever of an array is decreased to a few hundred nanometers (100-500 nm). In this context, the decrease of thermomechanical actuation efficiency requires a significantly improved tilt compensation system. In addition,

	as experimentally observed, also variations in tip height and stress-related pre-bending, which are in range of 100-300 nm, are introducing further variations in tip-sample spacing, which have to be compensated by the thermomechanical DC actuation. Thus, the combination of an insufficient tilt compensation system and the variations of tip heights in an array are consuming the actuation budget of the cantilever. In this context, we have demonstrated the patterning only with two neighboring cantilever of an array. The other two cantilever of the array were either out of range (no pattern visible) or too close to the surface (induced an initial tip crash), whereby the tip-sample variations were out of range of the thermomechanical DC-actuation [remark: In case of parallel AFM imaging tests this problem didn't occur since soft cantilever are applied, which are characterized by enlarged DC actuation ranges. In this case the actuation range was large enough in order to compensate the variations in tip-sample spacing of the individual cantilever]. Thus, as revealed the lithographic mode becomes much more challenging as the imaging mode with "Quattro" cantilever arrays. Increased requirements on tilt compensation and tip height variations are necessary, which were not anticipated in the beginning. However, the lack of time at the end of the SNM project has restricted further improvements. Here, mainly the following obstacles has induced time delays the during development phase: • The fabrication of thick cantilever arrays took more time than anticipated and showed more tip failures than the soft (=thin) cantilever arrays fabricated initially (as reported in D1.8). • The wire bonding of the Quattro cantilever chip for lithography was challenging, time-consuming and very vulnerable to errors. • Control electronics and software (feedback loops) are complex and thus becomes challenging (reported in detail below). • Suppression of mechanical and electrical crosstalk between individual cantilevers of an array. Details are reported below.
Explanation of Differences between Estimation	Significant unforeseen challenges have arisen during development of a closed loop FE-SPL system incorporating parallel imaging and lithography capability. Associated delays had impact onto the final outcome. Whereas the parallel imaging capability was successfully

and Realization	demonstrated, in lithographic mode the trade-off between cantilever stiffness and actuation efficiency was underestimated. This has resulted in significant change of requirements onto tilt compensation and cantilever array fabrication (reduction of variation of tip height and stress-related pre-bending). This final step was not possible to be achieved during the project duration. However, the principle of parallel field-emission scanning probe lithography was demonstrated by parallel exposure using two four cantilever.
Metrology comments	Since all cantilever of an array are actuated and measured independently, all cantilever of an array have to be individually calibrated. In particular, the Quattro cantilever system was calibrated by a home-made Si calibration sample. The traceability is ensured by calibration of the reference sample via the Nanopositioning and Measurement Machine at TUIL (http://www.sios.de/produkte/nanopositionier-und-nanomessmaschine/). Further on, the application of the presented cantilever array configuration in means of a scanning probe microscopy (SPM) system could lead to a misinterpretation of the read-out signal measured by the piezoresistive bridge when using a constant conversion factor. In order to measure exactly the deflection amplitude during scanning we apply the DC signal received from the piezoresistive deflection sensor. A calibration of this signal (V → nm conversion factor) is required. In contrast to an isotropic Euler Bernoulli beam model, the model applied shows a non-constant ratio between the conversion factor for the first two eigenmodes. Thus, an individual calibration of the beams of an array by using only the first Eigen frequencies is not sufficient. As a result, a conversion factor for each mode should be used in order to minimize the error for tip motion estimation. In these terms, we transduced the cantilever of the array mainly at first eigenfrequency.
References	/

1. FE-SPL technology platform – Mechanical set-up:

TUIL designed, fabricated and assembled a FE-SPL technology platform able to operate with four individually controlled cantilevers of a cantilever array. The so called "Quattro" cantilever system platform is summarized in Figure 1. The general system is based on the single cantilever alpha SPL-tool (ref. 1st and 2nd year report and D1.3) with an adapted cantilever holder, scanner, electronics, FPGA controller and preliminary user interface. The applied piezo-scanning unit has a scanning range of 200 x 200 x 20 µm [X/Y/Z]. Since the tip-to-tip distance of the cantilever array is 125 µm an overlap of single scanning/writing fields is given. A high precision tilt correction mechanism, which is capable to compensate a tilt of < 3° between sample surface and Quattro cantilever array with a resolution of 0.25°, was integrated. The tilt correction is connected with an automatic "cantilever array to sample" approach unit.

In order to manage the electrical connection (7 connections per cantilever + 1 substrate contact → in total 29 connections for a 4 cantilever chip has to be handled) and mounting of the Quattro cantilever array a novel interface was developed. The evolved Quattro cantilever interface is summarized in Figure 2. The cantilever chip is mounted on a compact holder (Figure 2-a). The electrical interface is established by wire bonding, Figure 2-c. Since the board is connected directly to the scanner unit it needs to have a small size and weight. An easy exchange of the cantilever array board was established by an pull-push principle. In addition, the four channel pre-amplifier electronics (ultra-low noise, band width DC – 2MHz @ gain 100) has to be placed close to the array. Therefore, a specially designed pre-amplifier board (Figure 2-b) was developed, which integrates an easy push-pull cantilever array exchange mechanism. In this context, the board-to-board interface ensures an electrical connection as well as a mechanical mounting of the cantilever array (Figure 2-d).

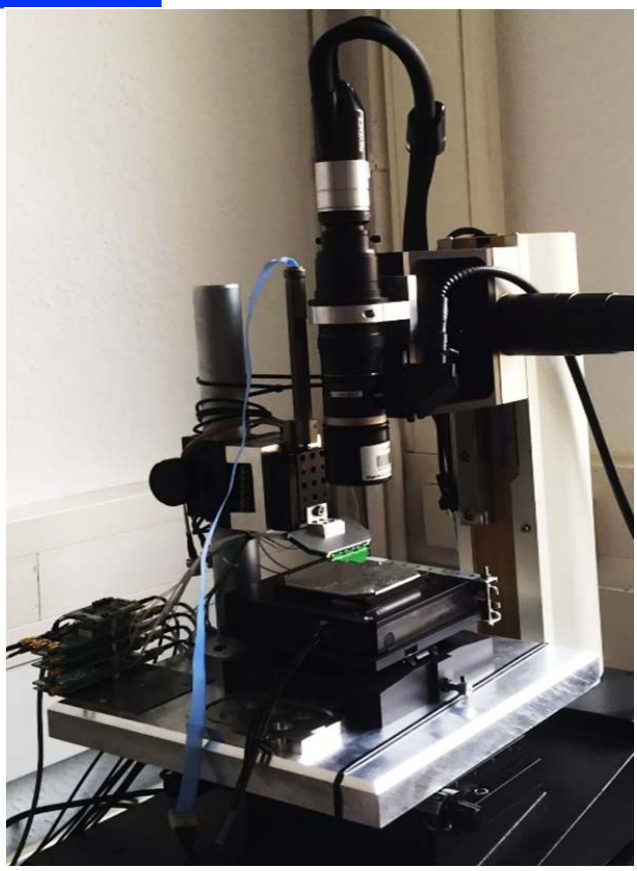

a) Experimental set-up for Quattro cantilever application tests.

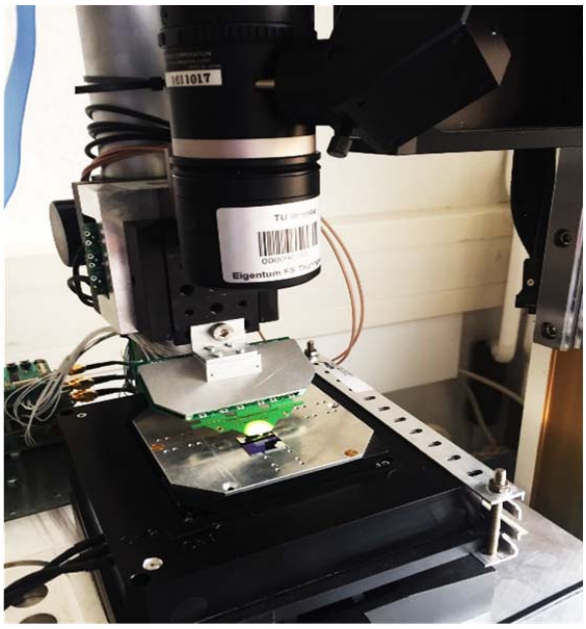

b) Zoom-in view of the Quattro cantilever holder, approach motor, bottom scanner equipped with tilt-compensation unit.

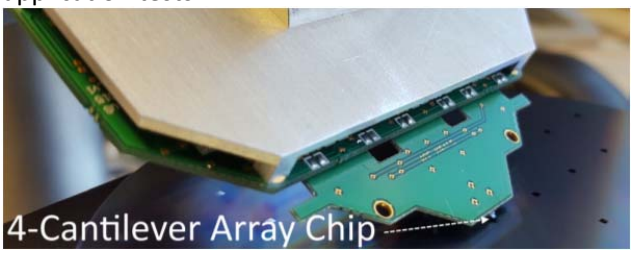

c) 4 Cantilever chip mounted on exchangeable PCB board. The analogue front-end is placed close to the cantilever chip in order to minimize the noise.

d) Camera image showing the SNM-"Quattro"-chip backside overlaid with the sample surface.

Figure 1. Experimental set-up of the Quattro-cantilever FE-SPL technology platform.

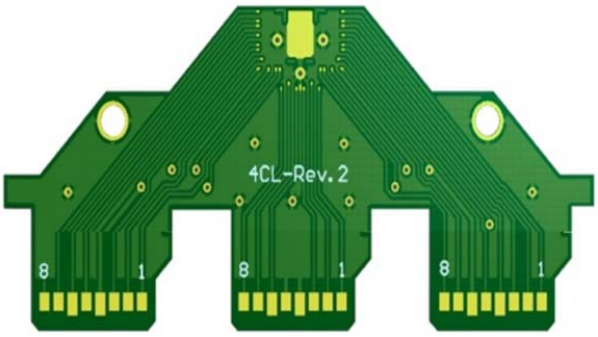

a) Quattro cantilever holder board

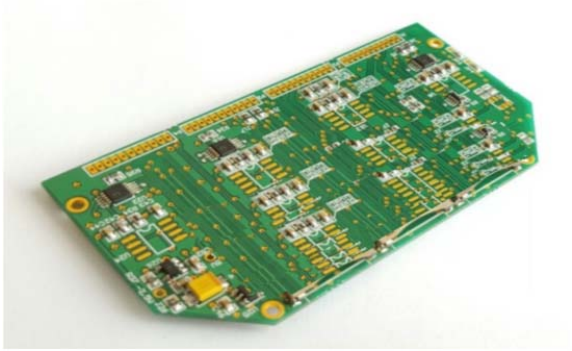

b) Four channel pre-amplifier board mounted directly onto the XYZ-scanner unit (chip holder is plugged in at the backside of the board)

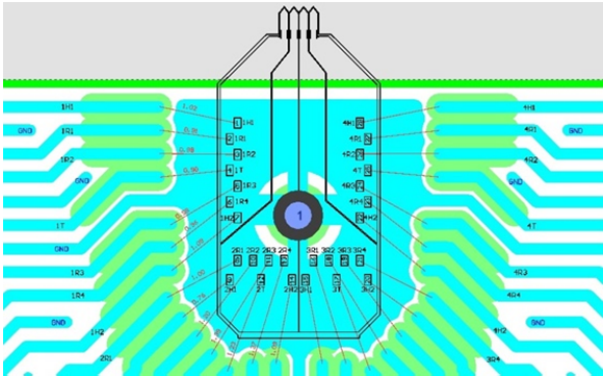

c) Bonding diagram of the Quattro cantilever chip (in total 29 connections are bonded)

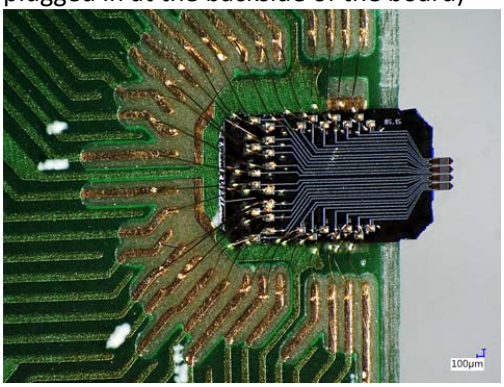

d) Wire bonded Quattro cantilever chip, mounted on the Quattro cantilever holder board (a).

Figure 2. Quattro cantilever interface

2. Concept of parallel active cantilever arrays integrating individual thermomechanical actuator and piezoresistive deflection sensor:

The Quattro cantilever array combines four active cantilever, shown in Figure 3. Each cantilever integrates a thermomechanical transducer and piezoresistive readout. An ultra-sharp cantilever tip with a radius of curvature between 15 +/-3nm is specially designed to enable both imaging and low-energy electron lithography capabilities of each individual active cantilever probe. The design and fabrication of the cantilever array was described in detail in a previous deliverable report D1.8 (“Four cantilever array with integrated nano-tips fabricated”).

The piezoresistive read-out technique is applied for static as well as for dynamic measurements of the cantilever deflection. The advantage with respect to conventional optical techniques is that neither additional optical components nor a laser alignment is needed. In fact, the weight of the scanning

cantilever head can be significantly reduced. On the other hand, the piezoresistive read-out secures routinely atomic resolution and remarkable high scanning speeds.

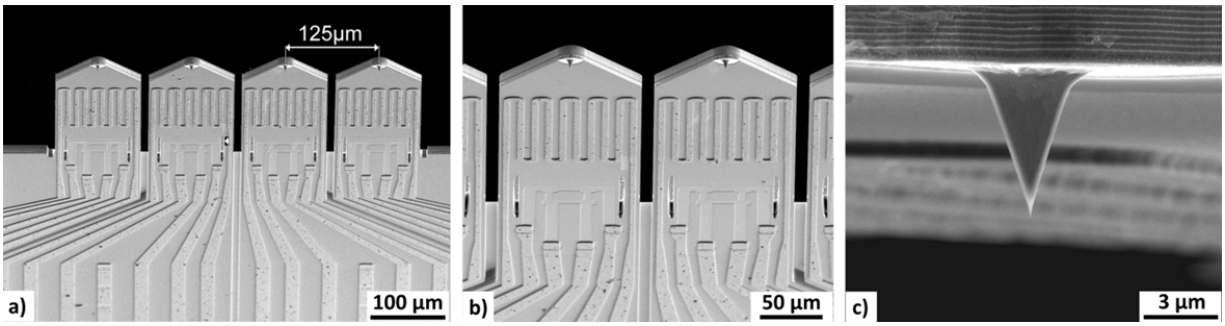

Figure 3. SEM image of the active "Quattro" cantilever array. Each cantilever includes a thermomechanical transducer used for static and dynamic deflection. The deflection is controlled by a piezoresistive readout. The cantilevers are equipped with sharp tips formed by highly doped Silicon. The distance (pitch) between the neighboring cantilever is approx. 125 µm.

Each cantilever of the array is excited individually by applying a voltage to its actuator. The excitation signal consists of a static DC component and a dynamic AC sine-wave component Eq. (1).

$$v(t) = V_{dc} + V_{ac}.\sin(\omega t) \qquad (1),$$

where ω is the AC voltage frequency. The dissipated heat in the thermomechanical actuator causes a cantilever deflection, which linearly depends on the heating power, given by Eq. (2):

$$p(t) = \frac{v(t)^2}{R_{heater}} = \frac{1}{R_{heater}}\left(2V_{dc}V_{ac}\sin(\omega t) - \frac{V_{ac}^2}{2}\cos(2\omega t) + \left(V_{dc}^2 + \frac{V_{ac}^2}{2}\right)\right) \qquad (2),$$

where *p(t)* is the heating power and R_{heater} is the ohmic resistance of the actuator. In case of a driving AC frequency of one half of the resonance frequency ω_0, the amplitude of the cantilever oscillation at the resonance is independent of the applied DC voltage, as seen from Eq. (3):

$$p(t) = \frac{v(t)^2}{R_{heater}} = \frac{1}{R_{heater}}\left(2V_{dc}V_{ac}\sin\left(\frac{\omega_0}{2}t\right) - \frac{V_{ac}^2}{2}\cos(\omega_0 t) + \left(V_{dc}^2 + \frac{V_{ac}^2}{2}\right)\right) \qquad (3)$$

In that case the DC voltage applied to the heater is used for a static bending control of each cantilever, whereas the AC amplitude is independent from the DC bending. Typically the z-piezo stack actuator tracks the topography in the z-direction and needs to be much faster than the highest spatial frequency of the sample. In case of "Quattro" cantilever operation the thermal actuator is used for both an AC excitation of the cantilever in resonance as well as applying a feedback signal for topography. Thereby, the quasi-static DC (frequencies ≤ 1 kHz) actuation acts as feedback signal for topography tracking. Combined with the high frequency actuation (at $\omega_0/2$) for a resonant excitation of the cantilever an

unique capability of the "Quattro" array for parallel operation is given. The possibility of controlling each probe individually is the most important feature used to independently track the topography by each active cantilever of the array. Figure 4 illustrates the individual actuation of an active cantilever in a cantilever array. The entire range of the static bending of the cantilever is used in order to adjust individually the working set-point as well as to track the surface topography. The working scheme is illustrated in Figure 5 and Figure 6, respectively.

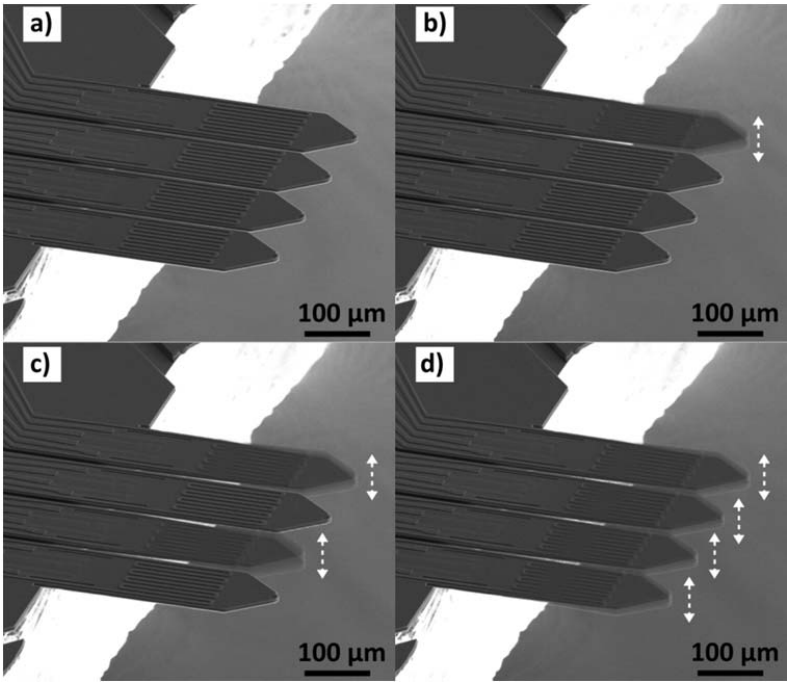

Figure 4. Individual actuation of cantilever in an active-probe Quattro-array: (a) All cantilevers are static; (b) Only the first cantilever (counted from top) is actuated; (c) First and third cantilever actuated; (c) All four cantilever actuated.

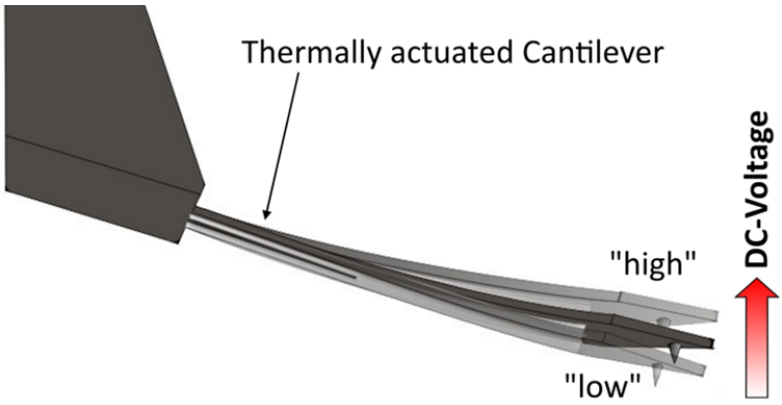

Figure 5. Schematic illustration of different static cantilever deflection cases of an active cantilever as function of the DC voltage component applied to the thermomechanical actuator.

In our system the amplitude of the high-frequency excitation is in the range of up to tens of nm, while the dynamic range of the slow DC bending used for tracking of the topography depends on the cantilever specification. Here, the particular design defines the thermomechanical actuation efficiency, e.g. soft cantilever give a higher efficiency, but they are more prone to the parasitic electrostatic actuation. Typically, a quasi-static movement range of up to 5 µm in case of soft cantilever is given. As revealed

during the experimental phase, in case of stiff cantilever, which are required for lithographic application, the actuation efficiency is decreased achieving only a quasi-static bending range of up to 500 nm. Here, AC amplitudes in the single nm range are applied. The frequency bandwidth of the AC vibration is up to 4 MHz while the bandwidth of the low-frequency bending signal is in the range of 0.5-1 kHz. The possibility to actuate each cantilever individually by applying a DC voltage and keeping the amplitude of oscillation at the resonance frequency constant by using the half-resonance mode is the basis for the realization of a parallel four-channel tracking of the sample topography in a vertical (Z) direction. Thereby, the oscillation amplitude of each cantilever measured as AC voltage at the output of piezoresistive bridge serves as Z-feedback signal while the driving DC voltage applied to the actuator keeps the distance between the tip and surface constant. The latter one is also used as the topographic information signal. In total, each cantilever has integrated its own AC-actuation, DC-deflection as well as deflection read-out unit enabling an individual operation of each cantilever of an array system.

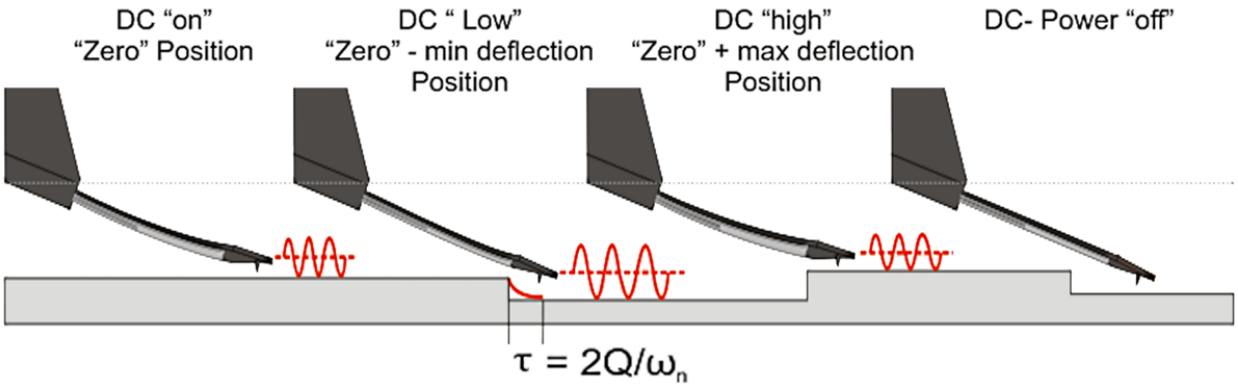

Figure 6. Application of different working DC-deflections during surface scanning. Each cantilever from the array is being individually controlled by means of a DC-deflection control.

3. FE-SPL technology platform – Implementation of electronics & software:

The development of the preliminary four-channel FE-SPL controller and software was summarized in frame of the deliverable report D1.5. The implemented high throughput data transfer system for mask data handling and data transfer is described in D1.9. During integration of electronics, software and hardware several further developments were required, which are described in the following. Thereby, unforeseen issues were faced during integration, which were solved but had induced some further delays in final implementation.

The multi-channel FE-SPL controller architecture for the “Quattro” cantilever array comprises of four identical channels each implementing high-speed AFM imaging and nano-lithography functionality. The implemented controller architecture is summarized in Figure 7. One of the channels (named master channel) has integrated additional mid-speed interfaces responsible for XY scanning and Z approach of the “Quattro” head. The physical construction of the controller uses common-bus architecture, allowing multiple boards to be plugged in the common base motherboard. The motherboard distributes all supply voltages, the low-speed SPI signals, as well as the synchronization digital lines. The AFM/FE-SPL part of each single-channel board provides full two-channel functionality of every “Quattro” cantilever for excitation and feedback signal processing. Two high-speed analogue and mixed-signal front-ends are implemented on the board. One is used for AFM imaging and the second for implementing the lithography feedback. The industrial-grade FPGA core module implements all-digital control blocks as well as the transport and network layer of the data transfer system.

The AFM imaging functionality, summarized in block diagram Figure 8, is realized by a high-speed mixed signal interface providing up to 60 dB amplification of the feedback signal from the sensor with a bandwidth of 2 MHz, following by a 16 bit, 100 Msps analogue to digital conversion. A 10 MHz, 16 bit locking amplifier referenced by the actuation frequency is further used to suppress the electronic and electromechanical noises, thus providing a resolved amplitude and phase of the feedback sine wave signal. The precise regulation of the DC bending of each sensor from the cantilever array is used for controlling the constant tip-surface distance during the AFM imaging. A 1 MHz PID controller provides the 18 bit output for vertical (Z) regulation of the cantilever which is fed to the 16 bit DAC for the sensor DC bending voltage. The sensor excitation is implemented by means of a programmable voltage supply from 0 to -2.5 V for the piezoresistive bridge and an AC excitation channel realized by a 0.01 Hz resolution 5 MHz DDS generator. The output driver for each thermomechanical actuator can drive 15 Ohm load by up to 35 mA in a bandwidth of DC up to 5 MHz. For nanolithography functionality,

summarized in Figure 9, a high speed 100 MHz, 16 bit mixed signal interface is used to perform a current to voltage conversion of the tip current and subsequent analogue to digital conversion. The low-noise current to voltage converter has a bandwidth of 2 kHz and 5 mV/pA transfer ratio. The very small (<3 fA) bias current allows extremely small tip currents to be measured during the lithography operation. The digitized current feedback signal is then fed to the same PID digital block which flexible architecture provides a dual-purpose usage by reprogramming its parameters. The output of the PID controller is used as a driving signal for the DC bending of the cantilever in a static mode. The programmable high-voltage source is used to provide a bias voltage for the substrate in a lithography mode. The synchronization module in AFM imaging mode is responsible for (i) simultaneous approach and individual excitation and Z-control of each cantilever of the array and (ii) synchronization of the XY data coming from the different boards. The latest is realized by sending X and Y synchronization values for each N-th line, where N can be chosen per the image resolution and scan speed. All parameters relevant to each working mode are sending through the communication interface and stored in the internal registers of the FPGA module. The image data are temporary kept in a 512 Mbits memory buffer capable of holding 1024 X 4096 pixel image frame. The high throughput data transfer system allows a theoretical speed of 2035 lines/s to be achieved using 1 Gb Ethernet line which capacity exceed by a long way all practical applications of the system.

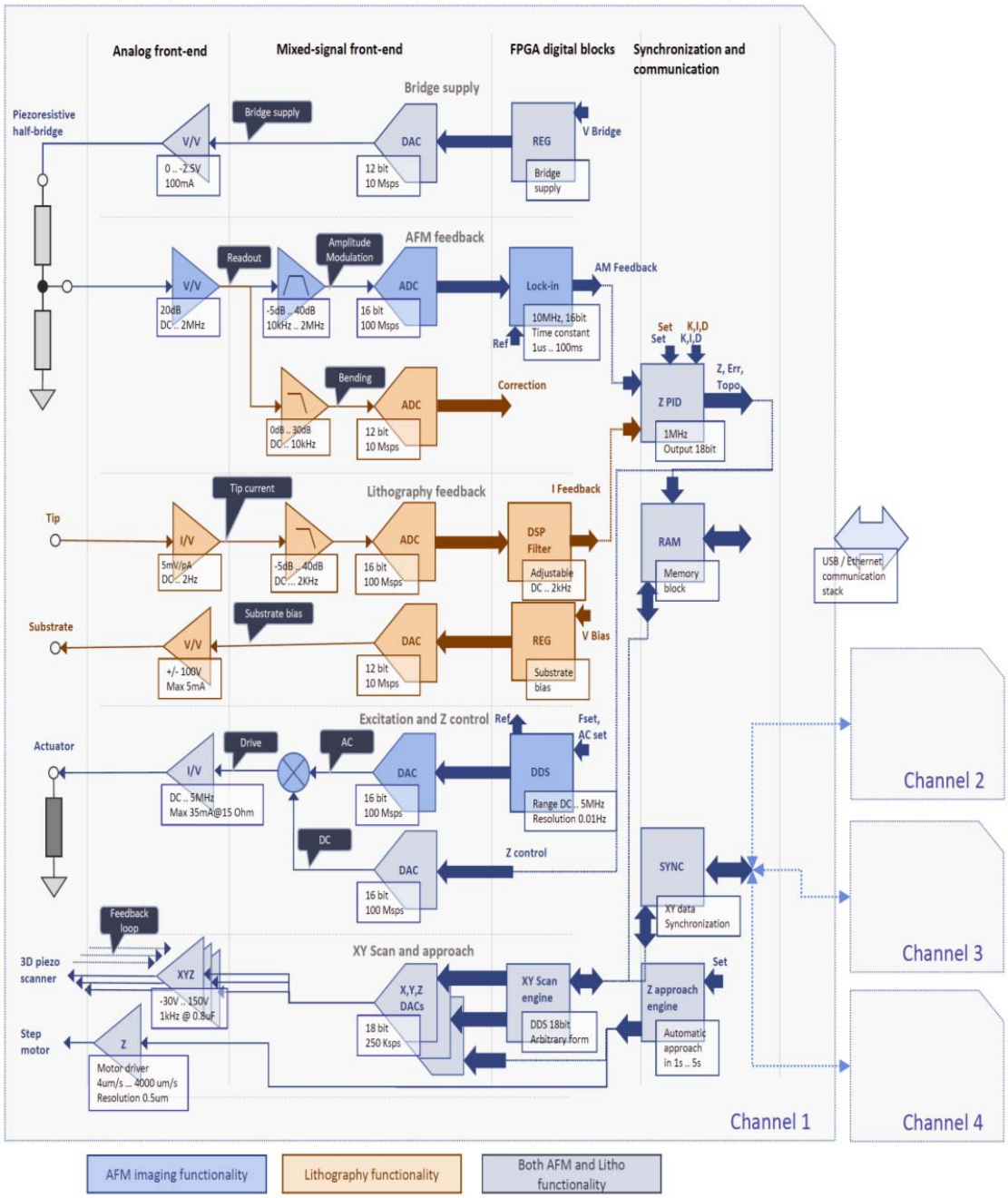

Figure 7. The multi-channel FE-SPL controller architecture comprises four identical channels each implementing high-speed AFM imaging functionality and SPL functionality.

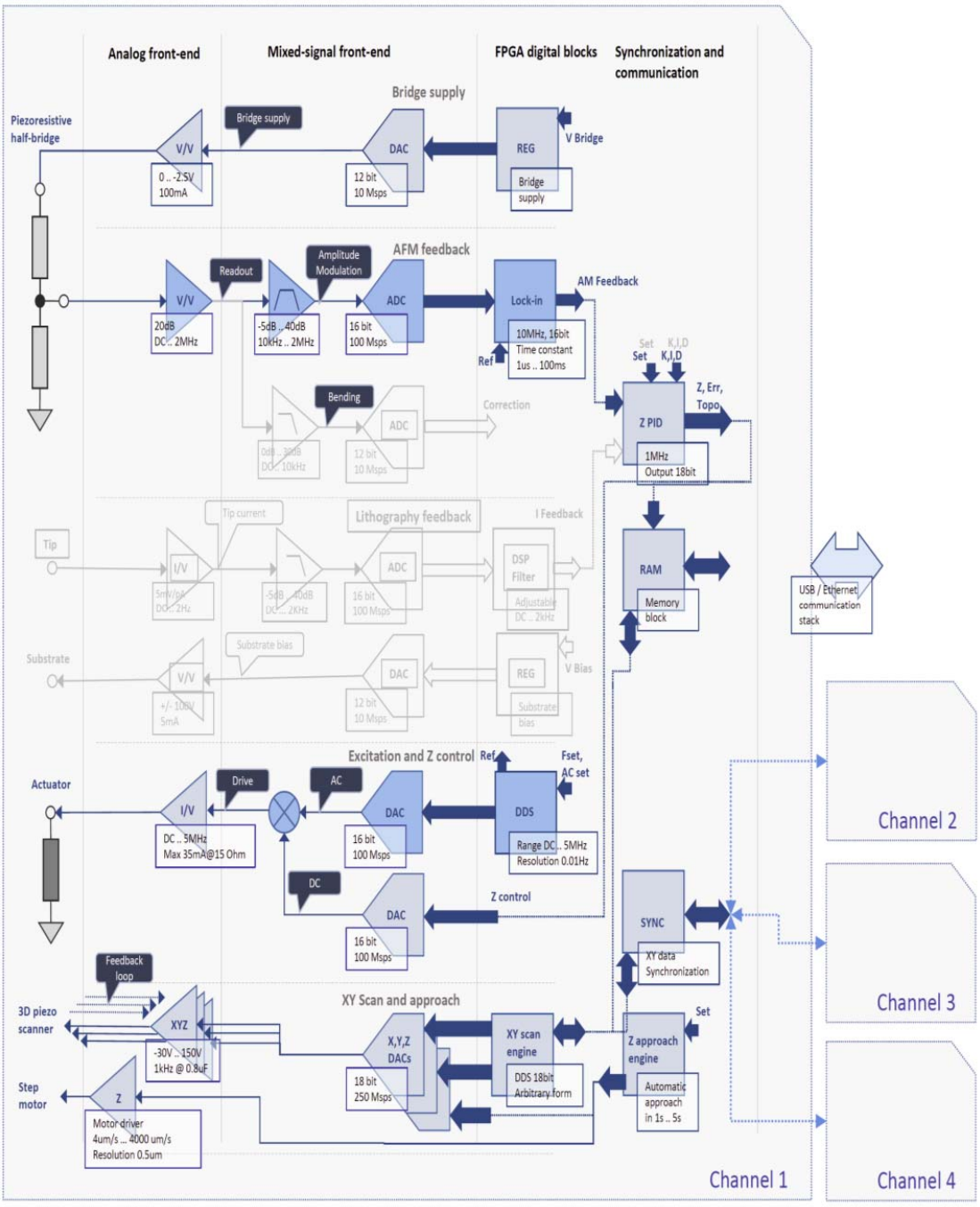

Figure 8. The multi-channel controller part used for AFM parallel imaging functionality.

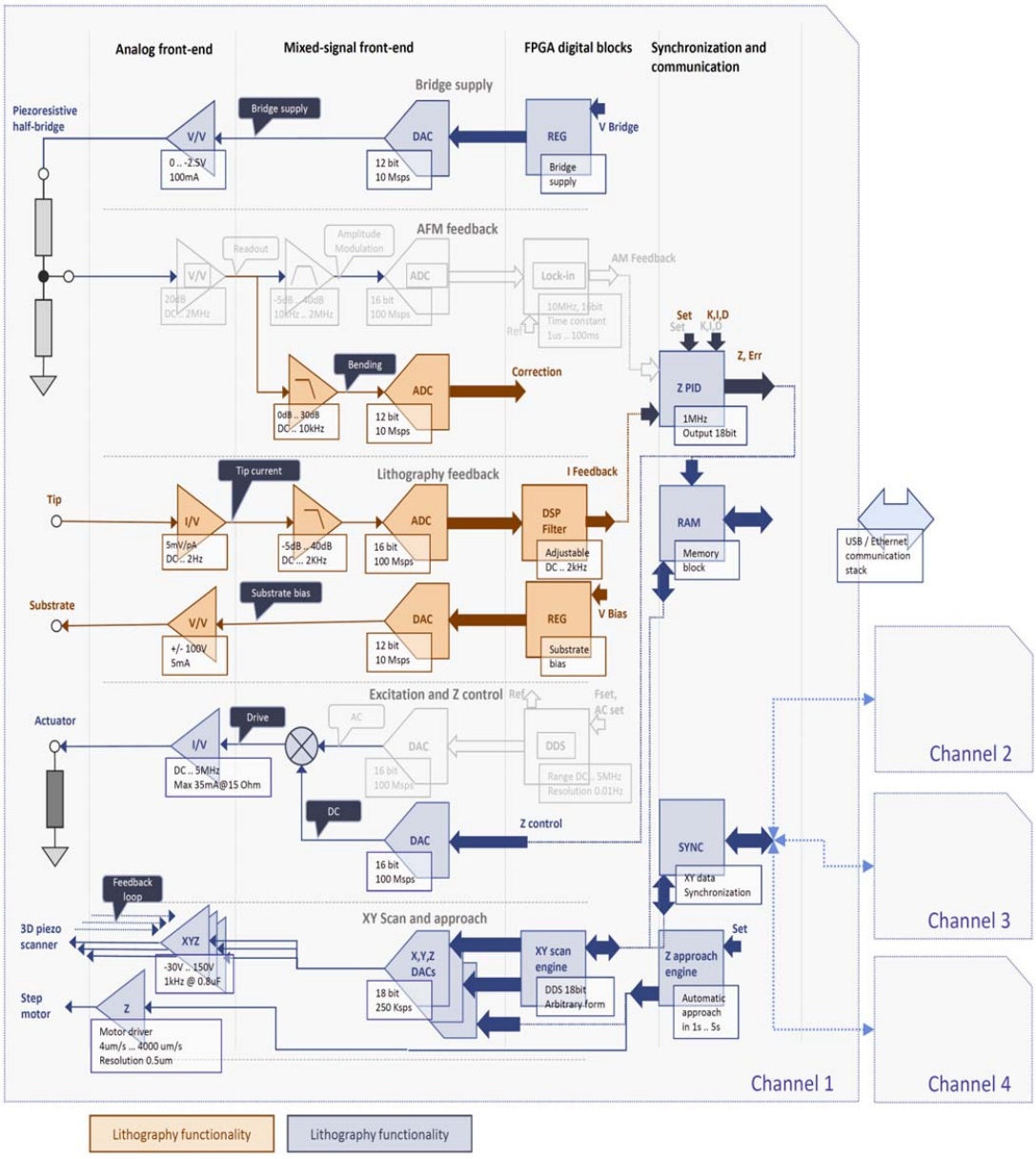

Figure 9. The multi-channel controller part used for parallel FE-SPL patterning functionality (current regulation).

According to the principle of operation (section 2), each cantilever is individually actuated by applying a DC voltage and keeping the amplitude of oscillation at the resonance frequency constant by using the half-resonance mode. This is the basis for the realization of a parallel four-channel tracking of the sample topography in a vertical (Z) direction. Thereby, the oscillation amplitude of each cantilever, measured as AC voltage at the output of piezoresistive bridge, serves as Z-feedback signal while the driving DC voltage applied to the actuator keeps the distance between the tip and surface constant. The latter one is also used as the topographic information signal. The basic idea behind is outlined in Figure 10. A Direct Digital Synthesis (DDS) unit generates the AC part of the actuator driving signal running on $\omega_0/2$ (ω_0 = resonance

frequency of the cantilever). This part is summed up with the DC voltage, which is setting the cantilever bending. Thereby, the DC components are not affecting the amplitude of the mechanical oscillation, or vice versa (ref. Eq. 3). The output AC signal from the cantilever's piezoresistive bridge is pre-amplified and then fed into a fast Lock-in amplifier (the reference signal comes from the same DDS generator). The amplitude output of the Lock-in amplifier serves as Z-feedback signal. In accordance, the DC-bending controller sets a DC voltage applied to the actuator.

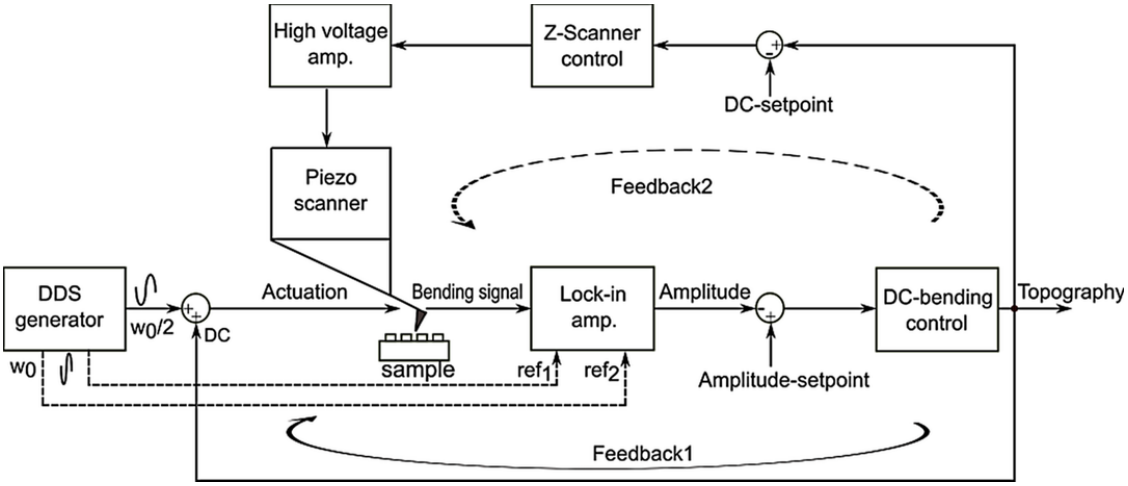

Figure 10. Functional diagram of the active cantilever regulation loops.

Each individual cantilever in the array gives a Z-range of up to 5 µm (soft cantilever applied for imaging). The complete Z-feedback function is aimed not only to track the topography details, but also to compensate the overall system drift caused by sample slope, temperature drift, etc. The latter one can be up to the Z-range of the cantilever. For that reason a second feedback loop ("Feedback-2" drawn Figure 10) is implemented. While "Feedback-1" tracks the topography, "Feedback-2" determines the DC voltage set-point for "Feedback-1" and keeps it constant. The output of "Feedback-2" controller is used as a compensation signal for the Z-piezoscanner. The low-frequency nature of the system drift determines the bandwidth of the "Feedback-2" loop controller (5 Hz). Table I summarizes the typical parameters of the two control loops operated. Both regulation loops are implemented in the FPGA controller.

TABLE I. Summary of the two feedback loops used for AFM imaging operation.

Controller Loop	Purpose	Resolution	Bandwidth
Feedback-1	Tracking of the topography	16bits	1 - 10kHz, depending on application
Feedback-2	Cantilever array approach & System drift compensation	16bits	5Hz

One Feedback-1–type controller is realized for each channel. Since four channels are required corresponding to each cantilever of the array; in total, four Feedback-1–type controllers are implemented and synchronized. In contrast, only a single common Feedback-2–type controller is required for the entire system.

Challenges and difficulties faced during the development: Building the system with four parallel working probes realized on a common substrate was a challenging task which requires specific problems in sensor design, mechanical setup and control electronics and software to be solved. Most of the challenges were carefully considered by the team whilst building the initial specification and system architecture (D1.1). However, the importance of each specific problem and the related real resources spent for its solving were fully realized during the final task implementation. Regarding the control electronics, the most important problems which the team faced during the development were:

a. **Development and implementation of a procedure for simultaneous approach of four cantilevers, whereby an optimal set point for all cantilevers is provided keeping the required dynamic range of Z regulation (= static deflection range of the cantilever by a DC voltage onto the heater) for each single cantilever:**

   In a single cantilever set-up the vertical approach of the probe as well as the tip-sample distance control can be realized by the Z piezoscanning unit. This kind of technique is not working in the multi-cantilever case because of the non-equality of the absolute Z-positions of each individual cantilever. Thus, there are differences in the relative Z-position between the four active cantilever, which are introduced by (a) variation in tip heights, (b) variation in stress-dependent pre-deflections, and (c) remaining cantilever array tilt compared to the sample surface.

   Therefore, an alternative technique for the Z-control had to be developed which combines the AC actuation, DC bending and compensating Z-piezo movement in a complete stable working system. The minimal target resolutions initially set were 15 bits for the Z-control loops and 14 bits for the AC actuation. Several theoretically suitable solutions were explored, practically implemented and tested in preliminary FE-SPL setups. An analysis of the system behavior was performed and a final solution was developed. Here, a 16 bit resolution for the Z-control of each cantilever was chosen, determined the final hardware design and digital FPGA implementation of this part.

b. **Synchronization of the data coming in parallel manner from each of the four cantilever in the time domain:**

   The synchronization is intended to solve the XY misalignment of the data coming from different boards, which is caused by the non-equality of the local clock frequencies for each FPGA board (up

to 50 ppm). The solution of this problem should consider the maximum propagation speed between the boards, as well as the various scanning algorithms, which are realized in the controller. Various solutions of this problem were investigated, including common master 100 MHz clock, single X-line synchronization, spatial recognition of the data and single line synchronization for the X and Y lines. Finally, the most reliable solution was selected and the performance of the system according to the specification was confirmed during final experiments.

c. **Equalization of the phase and amplitude characteristics of the front-end of all high-speed mixed-signal interfaces:**

The Z-regulation of the cantilever requires two feedback loops to be realized. One is tracking the topography by changing dynamically the DC bending of the cantilever. A second loop is compensating the entire system drift caused by the sample slope, temperature deviations, etc. The applied approach allows a working Z-range of 2-5 µm to be achieved for each of the cantilever in the Quattro cantilever array. In such a system the phase delays of the readout signal impact significantly the reaction of the system, especially in case of high-frequency cantilever. Special measurements were undertaken for optimal board design and component selection in order to minimize the deviations in the phase characteristics of different channels and to minimize the propagation delay of the digital signals. Additionally, dedicated controller phase delay blocks were implemented in the FPGA core. Although this problem was taken into account during initial creation of the internal specification of the system, its significant impact on the performance of the Z-regulation loop was unforeseen and was firstly visible during experiments using the assembled FE-SPL technology platform. Respectively, the related difficulties in creating the consistent solutions were not fully envisaged in the very beginning. This task has consumed significant resources. In the end, effective solutions were achieved at the end of the fourth year.

4. Investigation of crosstalk between cantilever of an array:

During initial experiments crosstalk between the cantilevers in the array was observed, which limits the parallel operation capability. Analysis of DC and AC characteristics of the “Quattro” array, for example resonance frequency shift, settling and response time have been done in order to handle the crosstalk problems.

The cantilever at resonant oscillation has a high sensitivity, accuracy and stability, but its mechanical resonance can be obscured by mechanical, thermal and electrical cross-talk between the own heater and

piezoresistor and neighboring ones. A stable and robust operation demands stringent requirements for actuation and detection electronics. In order to investigate the issues arising from crosstalk specific electronic simulation tools are applied. SPICE, a widely used program for electrical circuit analysis is common for this task. Here, a suitable electrical behavior model of the electro-mechanical sensor was simulated. By means of electro-mechanical and electro-thermal analogies the complete sensor system including the excitations and analysis electronics was investigated and optimized by a single simulator.

We developed an electrical network model of the thermal, mechanical and electrical characteristics of the cantilever including parasitic effects. For the heat transport 1- and 2-dimensional models were developed and evaluated. The mechanical pre-deflection and periodical vibrations as well as the resonance amplification were implemented, too. Additionally the model contains the electrical output signal determination of the piezoresistive sensor, which depends on the actuation, the cantilever dimensions and the sensor position and sensitivity. The model was verified with commonly used FEM-simulations (ANSYS) and measurements.

In this context we investigated the influence of the thermal actuation concerning the piezoresistor and second the thermal crosstalk between neighbor cantilevers. In order to reduce the complexity a two cantilever array model was applied as shown in Figure 11.

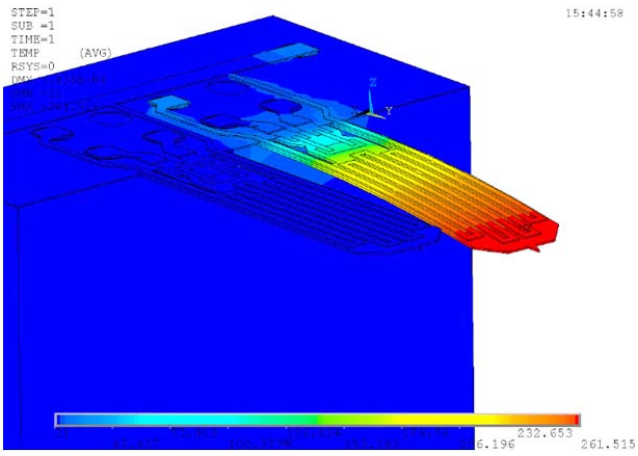

Figure 11. A two cantilever array model showing the thermal crosstalk between two neighboring cantilevers (one actuated and one passive).

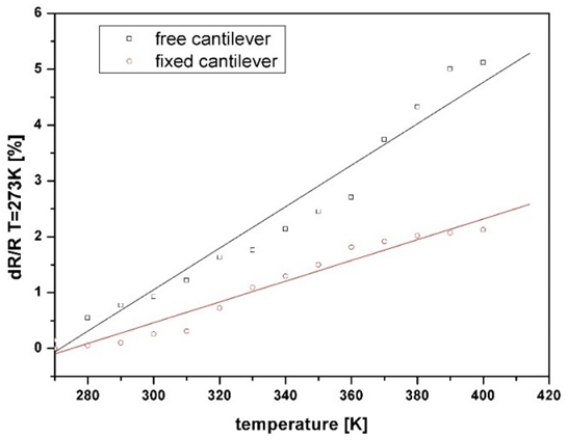

Figure 12. Relative resistance change for a fixed and free cantilever.

The piezoresistor are placed in that manner that there is no temperature compensation present like at resistor bridges. The DC-part of the thermal actuation, which controls the z-direction, generates hundred times higher temperature changes as the AC-part. These results from the low pass characteristic of the temperature transfer. For example, shown in Figure 11, one cantilever was heated with $P_{DC} = 80\,mW$.

A resulting temperature difference occurs across the cantilever of about 240 K. This results in a mean temperature increase of $\Delta T_{sensor} = 40\ K$ in the range of the piezoresistors in comparison to the non-heated cantilever. Such change in temperature induces a variation of the piezoresistor value according to:

$$\Delta R = \Delta T_{sensor} \cdot R \cdot TCR \tag{4}$$

where R is its resistance at room temperature and TCR its temperature coefficient of resistor. The TCR depends on temperature and doping dependence of hole mobility in boron doped silicon. The TCR was determined experimentally in a setup where a thermal induced restrain of the piezoresistor is negligible. In this terms only thermal changes of resistance was measured and the mechanical bending could be precluded. In Figure 12 the dependences of the piezoresistor value on the temperature is represented. In a good approximation it shows a linear temperature gradient. A constant TCR was determined: TCR = $3 \cdot 10^{-4}$ K^{-1}. Under operational conditions the resistance change is caused by the bimorph and the temperature change affect the resistance, described by

$$\frac{\Delta R}{R} = (TCR + bimorph)\Delta T \tag{5}$$

That means, thermal and mechanical resistance changes are measured during DC-actuation.

Equivalent circuit model applied:

The ***heat transfer*** to the cantilever depends on the heating voltage u according to

$$\begin{aligned} P &= \frac{V^2}{R_{heater}} = \frac{\left[V_{DC} + V_{AC} \cdot \sin(\omega t)\right]^2}{R_{heater}} \\ &= \frac{1}{R_{heater}} \cdot \left[{V_{DC}}^2 + \frac{{V_{AC}}^2}{2} + 2 \cdot V_{DC} \cdot V_{AC} \cdot \sin(\omega t) - \frac{{V_{AC}}^2}{2} \cos(2\omega t) \right] \end{aligned} \tag{6}$$

With R_{heater} is the resistance of the actuator. The voltage consists of a periodical part with the frequency ω and the amplitude V_{AC} and a dc-offset V_{DC}. The second row of equation 6 shows that the heating power contains besides the constant part and the periodical part with the frequency ω a further periodical part with the double frequency 2ω. This is important, since a single resonance mode of the cantilever can be stimulated with the corresponding frequency or with the half one. Such a heat source can be modeled in SPICE with a polynomial current source. The calculation of the ***temperature distribution*** T(y,t) in the cantilever is carried out under simplified assumption. The length is much bigger

than the thickness (l » d), the temperature is in cross direction almost constant and radiation and convection losses are negligible. So the dimensions are reduced to a SISO (single-input single-output) model for the heat transfer. These can be described by the 1-dimensional heat conduction equation:

$$\rho \cdot c_q \cdot \frac{\partial T(y,t)}{\partial t} = \lambda \cdot \frac{\partial^2 T(y,t)}{\partial y^2} + p(y,t)\,. \qquad (7)$$

ρ is the specific density, c_q the specific heat capacity, λ the heat conductivity, y the position along the cantilever and p the heat transfer per volume unit by the electric heater. The Cauer RC ladder approach with grounded capacitors and floating resistors represents the physical meaning (Figure 13).

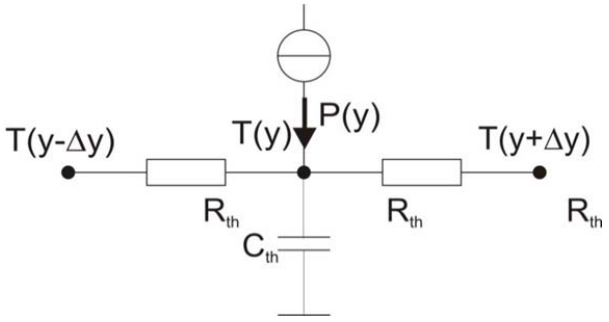

Figure 13. Equivalent electric schematic of a cantilever element to simulate the thermal behavior with SPICE.

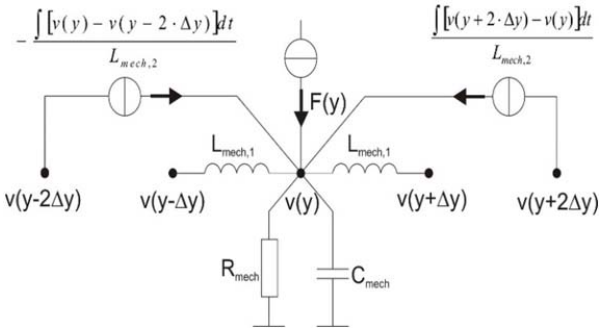

Figure 14. Equivalent electric schematic of a cantilever element to solve the differential equation of beam bending (l/L - spring constant equivalent, C – mass equivalent, 1/R – air damping equivalent)

The temperature T(y) of each cantilever causes a turning moment M(y) due to the different expansion coefficients of the layers. For a bimorph structure the moment depends on the temperature by:

$$M(y) = \frac{E_1 w_1 d_1 \cdot E_2 w_2 d_2}{E_1 w_1 d_1 + E_2 w_2 d_2} \cdot \frac{d_1 + d_2}{2} \cdot (\alpha_2 - \alpha_1) \cdot T(y)\,, \qquad (8)$$

Where E_i are the elasticity module, w_i the width, d_i the thickness of each layer. For a multi-layer structure a similar expression can be specified. The temperature caused moment distribution M(y) can be transformed in an equivalent external force load f(y) (force per unit length), because of:

$$\frac{\partial M(y)}{\partial y} = f(y) \cdot dy\,. \qquad (9)$$

That is inserted in the differential equation of beam bending after the Bernoulli theory

$$\frac{\partial^2}{\partial y^2}\cdot E\cdot I\cdot\frac{\partial^2 z}{\partial y^2}+\frac{\beta}{w}\cdot\frac{\partial z}{\partial t}+\rho\cdot w\cdot d\cdot\frac{\partial^2 z}{\partial t^2}=f(y,t)\ . \qquad (10)$$

In (8) E, I, z, ρ, w and d represent the elasticity module, the moment of inertia , the beam deflection, mass density, the width and the thickness of the beam at its longitudinal position y. β/w is the airflow damping factor. Starting from the discrete form of (8)

$$\begin{aligned}&\frac{4\cdot E\cdot I}{\Delta y^3}\cdot\{[z(y)-z(y-\Delta y)]-[z(y+\Delta y)-z(y)]\}+\\&\frac{E\cdot I}{\Delta y^3}\cdot\{[z(y+2\cdot\Delta y)-z(y)]-[z(y)-z(y-2\cdot\Delta y)]\}+\\&\frac{\beta\cdot\Delta y}{w}\frac{\partial z(y)}{\partial t}+\rho\cdot w\cdot d\cdot\Delta y\cdot\frac{\partial^2 z(y)}{\partial t^2}=F(y,t)\end{aligned} \qquad (11),$$

introducing the velocity $v=\partial z/\partial t$ and the parameters $L_{mech,1}$, $L_{mech,2}$, R_{mech} , C_{mech}

$$\begin{aligned}&\frac{\int[v(y)-v(y-\Delta y)]dt}{L_{mech,1}}-\frac{\int[v(y+\Delta y)-v(y)]dt}{L_{mech,1}}+\frac{\int[v(y+2\cdot\Delta y)-v(y)]dt}{L_{mech,2}}\\&-\frac{\int[v(y)-v(y-2\cdot\Delta y)]dt}{L_{mech,2}}+\frac{1}{R_{mech}}\cdot v(y)+C_{mech}\cdot\frac{\partial v(y)}{\partial t}=F(y,t)\end{aligned} \qquad (12),$$

an analogy to the electric circuit is achievable (the velocity corresponds to the electric voltage). Thus, an equivalent circuit model, summarized in Figure 14, can be formulated.

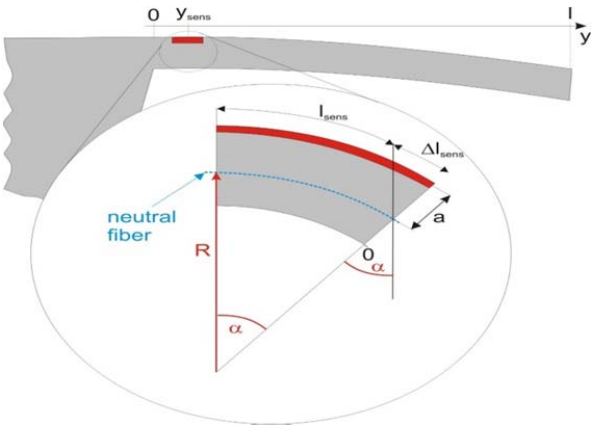

Figure 15. Strain at the piezoresistor due to the bending of the cantilever (R – the radius of curvature, a – the distance of the sensor to the neutral fiber of the beam).

Because of the heating characteristic including static and dynamic parts a time and position dependent force distribution F(y,t) acts along the cantilever and effects a static deflection superposed by oscillations z(y,t). It can be computed from the calculated velocity function

$$z(y,t) = \int_0^t v(y,\tilde{t})d\tilde{t} \ . \tag{13}$$

This is used to determine the strain and stress in the piezoresistive sensor and consequently its relative resistance change

$$\frac{\Delta R_{sens}}{R_{sens}} = \pi \cdot \sigma(y_{sens}) = \pi \cdot E \cdot \frac{\Delta l_{sens}}{l_{sens}} = \pi \cdot E \cdot \frac{a}{R(y_{sens})} = \pi \cdot E \cdot a \cdot \left.\frac{\partial^2 z(y)}{\partial y^2}\right|_{y=y_{sens}} \tag{14}$$

With π the piezoresistive coefficient in longitudinal direction, σ the stress near the cantilever surface at the sensor position y_{sens}, E the module of elasticity and a the vertical distance of the sensor from the neutral fiber (as shown in Figure 15).

Experiments:

The fabricated cantilevers were measured with a generator and a scope. Therefore, no additional pre-amplification was used to get real amplitudes and phases. Also the TCR (temperature coefficient of resistance) of the implanted sensor are determinate experimentally. Exemplarily the investigation of the frequency characteristics is shown in Figure 16. More precisely the rms sensor signal which corresponds to $\Delta R_{sens} / R_{sens}$ is represented. The simulated curve (red) contains the stress induced (due to the beam bending) as well as the temperature induced (temperature variation at the piezoresistor) resistance change. The electrical parasitic coupling which appears in the higher frequency range of experimental curve is not yet included. The peaks mark the frequencies of the heating voltage, where the cantilever is stimulated in resonant vibration. The temperature induced sensor signal (blue line) is for the represented example approximately 50% of the full sensor signal in the lower frequency range and must be regarded in the signal analysis. In the frequency region of the first harmonic the sensor signal becomes even smaller than its temperature induced part. Due to the phase shift of the mechanical oscillation the bending induced resistance change gets a phase shift of half a period. Hence both parts of the resistor change exhibit an anti-phase behavior and the total sensor signal is attenuated. Such an

investigation allows the evaluation of thermal crosstalk and can be simply extended to electrical crosstalk. The simulated results agree well with the experimental one.

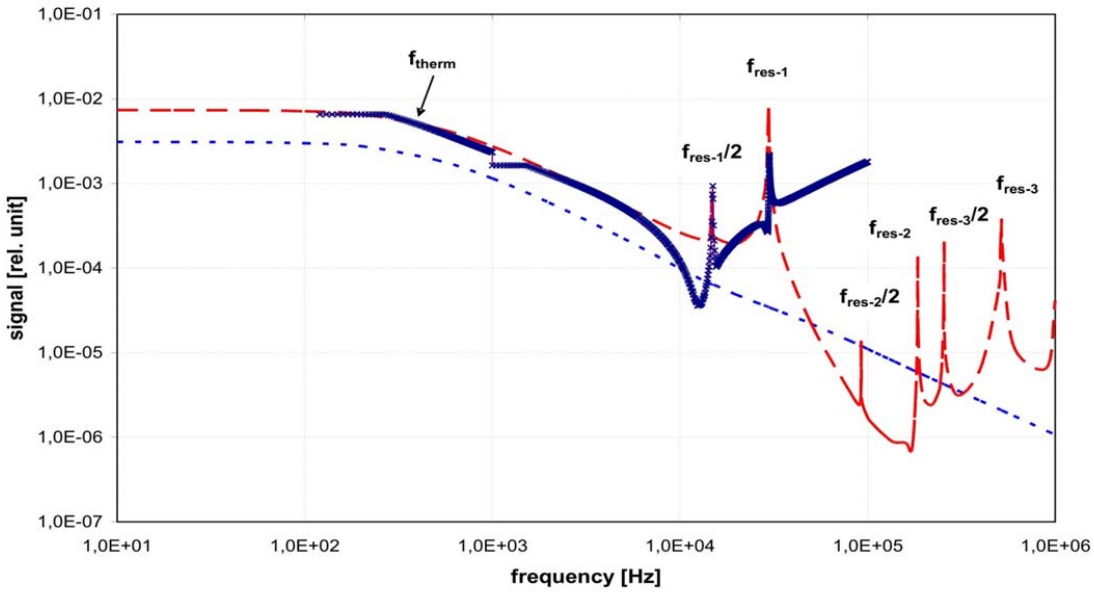

Figure 16. Frequency sweep of the rms sensor signal ($\Delta R_{sens}/R_{sens}$) versus heater frequency. The red (dashed) curve was simulated, the crosses are experimental results. f_{therm} is the cut-off frequency of thermal low pass. f_{res-1}, f_{res-2} and f_{res-3} are the resonance frequencies in the fundamental mode and the first and second harmonics. Each mode is actuated at the half of f_{res}. Additionally, the part of the rms sensor signal due to its TCR is plotted (blue dotted curve).

5. Demonstration of parallel imaging capability using Quattro cantilever arrays:

In frame of the deliverable the parallel imaging capability in AM-AFM mode was demonstrated. In particular, all four cantilever were applied simultaneously achieving the imaging a 0.5x0.2 mm scan area in a single scan with an effective scanning speed of 5.6 mm/s. In Figure 17, 18 and 19 results of high resolution measurements performed using the "Quattro" cantilever array are shown. In particular, in Figure 17 the parallel imaging of a Si line test structure is shown, Figure 18 demonstrates the merging of AFM scan fields covering a total image width of 0.5 mm and Figure 19 demonstrates atomic resolution capability in Z-direction by imaging of single layer steps on HOPG.

We applied amplitude modulation mode, in which the "Quattro" cantilevers are individually driven at their resonance frequency by applying a high-frequency signal to the thermomechanical actuator. Thereby, the vibration amplitude is a measure of the tip-sample interaction. The tip-surface distance is controlled by applying a low-frequency DC-bending signal to the thermomechanical actuator, as explained in section 2.

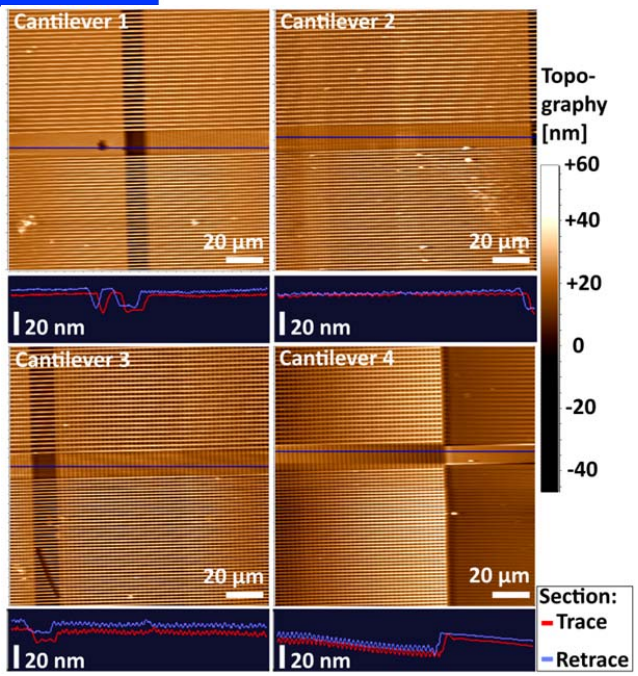

Figure 17. Parallel AFM imaging of Si line test structures by using the Quattro cantilever array. The simultaneous monitoring of all four cantilever of the array gives live information about the detected force-gradient of every cantilever-tip. Within the section graph trace and retrace of every cantilever is shown. The Si line test features are 700 nm wide and 14 nm in height. Amplitude modulation AFM mode was used at a single cantilever scanning speed of 10 lines/sec at a single image resolution of 512 pixel.

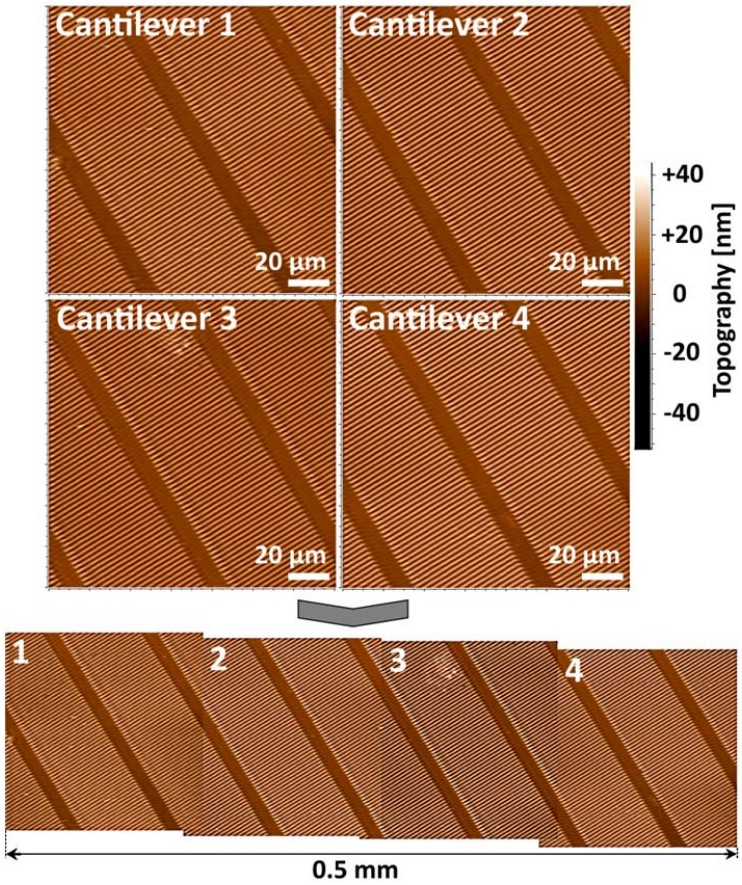

Figure 18. Merging of four AFM images obtained with the "Quattro" cantilever array into a single image. The merged scan covers a total image width of 0.5 mm. The Si test structure consists of 45 µm long and 14 nm high lines. The scanning speed was 10 lines/sec at 1028 pixels per line and channel in amplitude modulation mode. The data-size of the image was 256MBits.

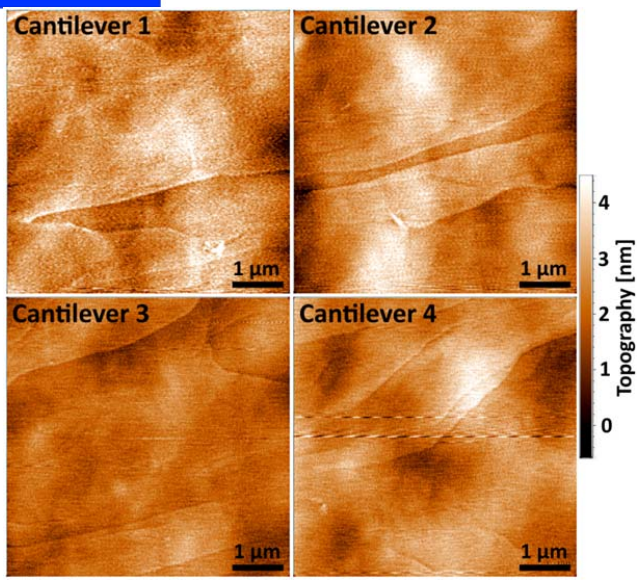

Figure 19. High resolution AFM imaging of HOPG by the Quattro cantilever array. A sub-nm resolution is achieved using a scanning speed of 10 lines/sec with 1028 pixels per line and channel (amplitude modulation mode). All four channels correspond to a single cantilever.

In such a way the static beam deflection is controlled in order to maintain defined amplitude of cantilever oscillation. This technique was used for first time and shows good capability to overcome cantilever crosstalk problems (ref. section 4). In our system an effective scanning speed of 5.6mm/sec is achieved. An update rate of the Z-controller of 20 MHz was applied. As shown in Figure 18 four fields were scanned simultaneously, whereby each field has a size of 140x140 µm. A typical scan speed of 10 lines/sec with a typical resolution of 512 pixel & lines were applied. In sum, the effective linear scanning speed (the speed of the single tip multiplied by four) is (4 * 140 µm) * 10 lines/sec = 5.6 mm/sec. For practical application of the four-channel system an estimation of the scanning speed and resolution versus the capability of the data transfer system is required. The cantilever scanner allows an area of 600 x 125 µm to be scanned with a speed of up to 100 lines/sec. Assuming a low-resolution scan targeted for an initial surface inspection a resolution of 1024x4096 pixel is applied, which gives an lateral resolution of 122.1 nm. The typical scan speed in this case is 20 lines/sec. In this case the entire frame is scanned within 51.2 sec. In our setup we are using 128 pixels payload and a 256 Mbit buffer size, which gives in total a transfer time of 279.45 ms for the overall data to be transmitted. Compared to the time required for scanning the transmission time is 183-times smaller. Thus, the speed of the data transfer is significantly higher than the scan speed, which allows practically a real-time imaging. Increasing the scan speed of up to 100 lines/sec does not alter this ratio noticeably. In fact, the transmission time is still 37-times higher. In case of higher resolution imaging the entire frame is organized in sub-frames, which fits the size of the memory buffers. For example, in order to achieve a 9.8 nm lateral resolution for a 600x125µm scan area an image size of 12800x51200 pixel is required. At 20 lines/sec scan speed the entire area is processed within 640 sec (10.7min). The total data amount is 40000 MBits, which are transferred in 157 packets of 256 MBits.

The results are reported partially in MS2. The corresponding results are published: Ahmad, A., Nikolov, N., Angelov, T., Ivanov, T., Reum, A., Atanasov, I., Guliyev, E., Ishchuk, V., Kaestner, M., Krivoshapkina, Y., Lenk, S., Lenk, C., Rangelow, I.W., Holz M., „Large area fast-AFM scanning with active “Quattro” cantilever arrays”, Journal of Vacuum Science and Technology B 34, 06KM03 (2016).

6. Tilt compensation issue vs. thermomechanical actuation efficiency and related DC actuation range:

A tilt compensation of 3° with a resolution of 0.25° between sample surface and Quattro cantilever array was planned and integrated. Taking into account a tip-to-tip lateral distance of neighboring cantilever of 125 µm of the Quattro cantilever array, a maximum of ≈2.2 µm difference in tip-sample spacing between the outermost cantilevers of an array is existing. Further on, variations of the individual cantilever of an array, associated with the fabrication process of the Quattro cantilever array (ref. D1.8), has to be taken into account. In particular, the fact that tips were formed by an optical lithography process, followed by an underetching process indicates limits in controllability of the tip height, tip width and tip placement. It can be concluded that the repeatability and reproducibility within an array is a critical issue. Further on, variations within the membrane formation step defining the final cantilever thickness are associated with tolerances. This leads to variations of the cantilever resonance frequency, spring constant as well as pre-bending (bending without thermal actuation). In sum, variations of the tip heights and stress-dependent pre-bending, which is in the range of up to 300 nm, the DC-(quasi-static) thermomechanical actuation budget of the outermost cantilever is reduced in total by 2.5 µm. In order to track the surface topography appropriately, this tip-sample spacing offset has to be compensated by the individual actuation.

In case of AFM imaging, summarized in section 5, relatively soft cantilever (approx. 22 N/m) as initially planned, were applied. In this case the measured quasi-static DC actuation amplitude, as shown in Figure 20, is up to 5 µm (induced at highest heating power). Thus, subtracting the maximum variations of tip-sample spacing between the outermost cantilever, an actuation range of 2.5 µm is remaining, which is sufficient for the small topographic changes measured typically (topographic changes of the samples applied are in the range ≤ 100 nm).

However, initial lithographic tests using soft cantilever reveals that the system is not sufficiently stable. Here, the parasitic electrostatic actuation as a result of the Coulomb force onto the cantilever beam causes significant instabilities of the field emission current regulation. Herein, the tip is attracted towards

the tip, whereas neither the restoring force of the cantilever beam nor the feedback regulation can compensate the abrupt tip-sample distance change. As a result, the tip crashes into the surface resulting in a mechanical tip-resist interaction (in case of slight pull-in) as well as in a tip-sample shortcut (in case of snap-in of the cantilever beam), exemplarily shown in Figure 21. More details and simulation about the Coulomb force onto the cantilever beam are summarized in section 7.

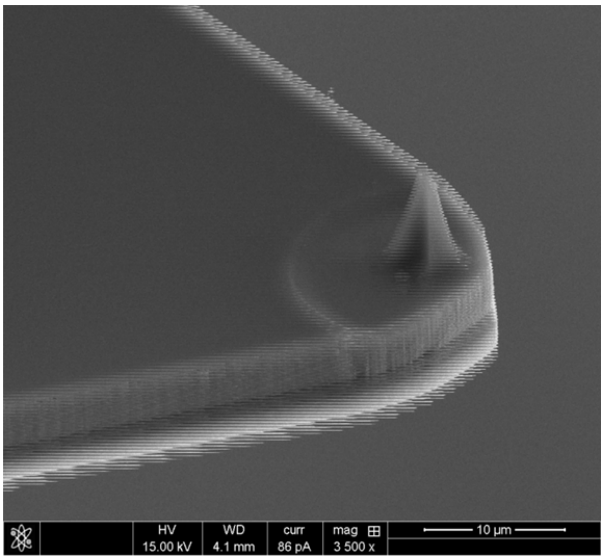

Figure 20. Measurement of the quasi-static (f<1 kHz) DC deflection in case of soft cantilever (k≈22 N/m) by in-situ SEM measurements. A deflection range of up to 5 µm is achievable.

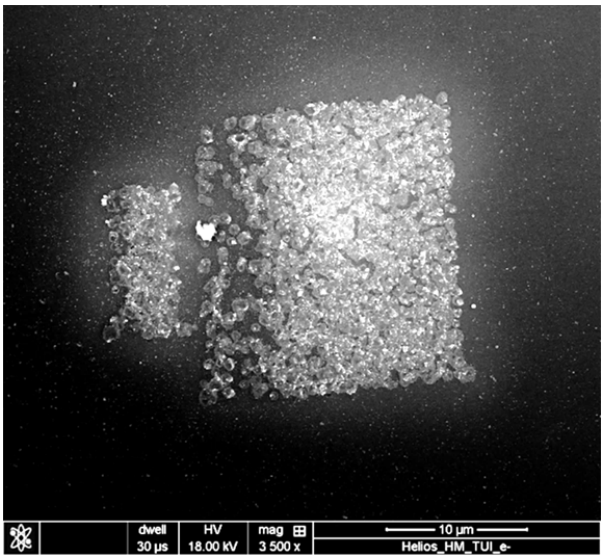

Figure 21. Example of current regulation instabilities induced by the parasitic electrostatic actuation. Increasing the cantilever stiffness circumvents the problem of pull-in of the cantilever beam.

In order to circumvent this problem Quattro cantilever arrays with increased cantilever stiffness (nom. ≈90 N/m) were fabricated. As drawback of this process the actuation efficiency is reduced, which results in a significantly decreased DC deflection range (more than predicted by simulations). In particular, a maximum DC deflection actuation range of ≤ 500 nm is determined, shown in Figure 22. As a result, the available actuation range is smaller than the variations in tip-sample spacing of an array of the outermost cantilever. Thus, the variation of the tip-sample spacing between the individual cantilever of an array is consuming the total quasi-static actuation budget. In other words, the tip-sample variations were out of range of the thermomechanical DC-actuation between the outermost cantilever of an array. As shown in section 8, we were only able to demonstrate the patterning with two neighboring cantilever of an array. The other two cantilever of the array were either out of range (no pattern visible) or too close to the surface (induces an initial tip crash).

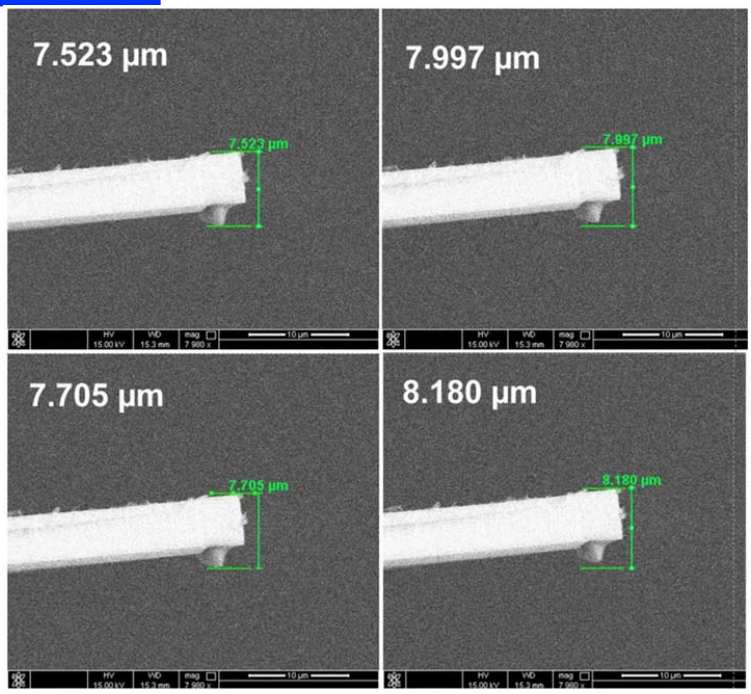

Figure 22. Determintation of the DC (quasi-static < 1 kHz) thermomechanical actuation range of stiff cantilever (k ≈ 90 N/m) by in-situ SEM. In total an actuation range of ≤ 500 nm is achievable.

In summary, the trade-off between cantilever stiffness, DC actuation efficiency and lithographic applicability was underestimated. In this context, a significantly improved tilt compensation system (tilt control resolution < 0.01°) as well as an improved tip height and cantilever pre-deflection control (variations < 50 nm) are required. However, this was not anticipated in the beginning. Due to some other time delays we were not able overcome this issue.

7. Simulation of parasitic electrostatic actuation:

a) Basic Considerations for the operation of cantilever arrays in FE-SPL mode:

When a voltage is applied between cantilever and substrate in order to perform FE-SPL an electrostatic attracting force is producing an electrostatic torque, which forces the cantilever to bend. The elastic restoring force acts against this force and restricts cantilever's motion. Illustrated in Figure 23, as long as the electrostatic force can be compensated by the elastic restoring force the system is in a steady state (static equilibrium). Upon reaching a certain critical gap or increasing the applied voltage to a critical value, the electrostatic force cannot be compensated any more by the mechanical restoring force. In this case the tip of the cantilever abruptly crashes into the surface, which is termed pull-in instability [*Batra R. C., Porfiri M. and Spinello D. 2007 Review of modeling electrostatically actuated*

microelectromechanical systems Smart Mater. Struct. ***16*** *R23–31*]. The corresponding values of the voltage and the tip-sample distance are called the pull-in voltage and the critical gap respectively.

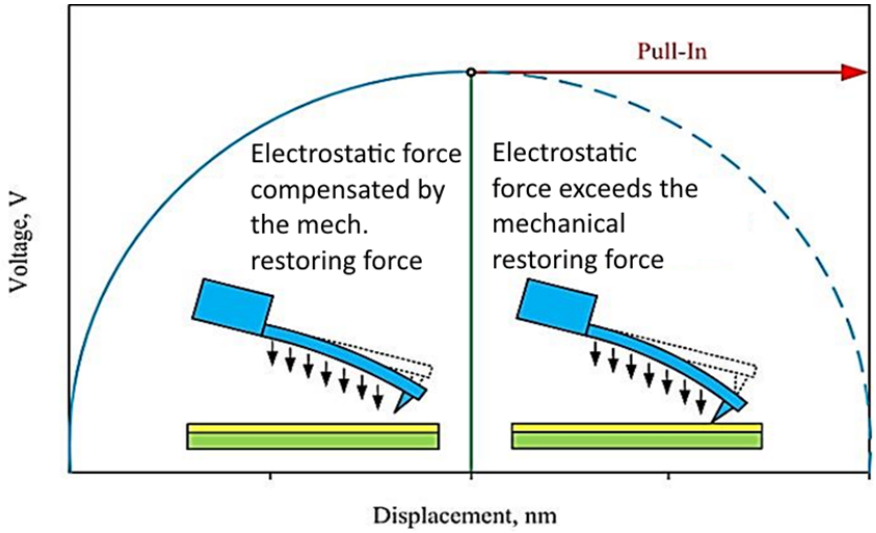

Figure 23. The equilibrium relationship between cantilever displacement and voltage (pull-in effect). The cause of pull-in phenomenon is due to the mixed dependence of the attractive electrostatic and restoring mechanical forces.

Furthermore, in the range, where the mechanical force compensates the electrostatic force, the large bending of the cantilever at nanoscale separations between tip and sample can yield a touching of the sample by the tip preventing a large bending. In the case of pull-in instability a shortening of the electric circuit for the Fowler-Nordheim emission occurs. In combination with the regulation feedback loop, which tries to work against this effect (the regulation is significantly too slow to compensate this effect), an oscillation of the cantilever can be generated by these effects leading to dramatic instabilities of emission control and thereof the lithographic control (Figure 21). Further on, both effects can lead to unexpected probe behaviour and destruction of the tip. Thus, determination of the optimal range of cantilever stiffness (=restoring force spring constant), applied voltage, cantilever angle and resulting deflection of the cantilever is of high importance for designing of the FE-SPL tool and the associated cantilever.

b) Simulations of Cantilever bending due to electrostatic force

We investigated theoretically and experimentally the occurrence of instabilities of the cantilever due to the electrostatic field in dependence of the critical tilting angle of the cantilever and the applied voltage used for the FN-field emission. Van der Waals effects are not considered in the simulations. Therefore, the cantilever is initially positioned above the substrate surface at a certain distance and with a certain angle given by the holder of the SPL tool (Figure 24). To evaluate the cantilever deflection it was necessary to calculate the spatial distribution of the deforming force in the electrostatic field. Firstly, the distribution of the static electric potential $\varphi(x, y, z)$ between the cantilever and the surface described by the Laplace equation has to be calculated:

$$\frac{\partial^2 \varphi}{\partial x^2} + \frac{\partial^2 \varphi}{\partial y^2} + \frac{\partial^2 \varphi}{\partial z^2} = 0 \quad , \tag{15}$$

where *x*, *y* and *z* are the spatial coordinates. The distribution of the electrostatic potential $\varphi(x, y, z)$ obtained as a result of the Laplace equation solution leads to the distribution of the electric field parameters using the known relations:

$$\begin{aligned} \mathbf{E} &= -\nabla \cdot \varphi \\ \mathbf{D} &= \varepsilon_0 \varepsilon_r \mathbf{E} \end{aligned} \quad , \tag{16}$$

where **E** – electric field strength, ∇ – Laplacian operator; **D** – electric displacement field, ε_0 – dielectric constant; ε_r – the relative permittivity. From the distribution of the electric field parameters it is possible to determine the impact force on the cantilever according to the Maxwell formula:

$$\vec{\mathbf{F}}_e = \int_S \mathbf{T} \cdot \vec{\mathbf{n}} ds \quad , \tag{17}$$

where $\vec{\mathbf{F}}_e$ – electrostatic force, S – surface bounding the cantilever, $\vec{\mathbf{n}}$ – the outward normal vector; **T** – Maxwell stress tensor:

$$\mathbf{T} = \mathbf{E}\mathbf{D}^T - \frac{1}{2}(\mathbf{E} \cdot \mathbf{D})\mathbf{I} \quad , \tag{18}$$

where **I** is the unit tensor and *T* the symbol of transposition. The displacement of the cantilever is calculated according to Navier's equation for the deformation of solids. Finite-element method is applied for the calculation of the electrostatic force and the displacement using the software COMSOL Multiphysics.

c) FEM MODEL TO ANALYZE THE BEHAVIOR OF CANTILEVER IN ELECTROSTATIC FIELD

Given the large difference in dimensions between the cantilever and tip size (Table II), a compromise has to be found between finite-element mesh quality and computational costs. Two types of FEM models were developed. Thereby, in one case a cantilever with tip is applied, whereas in a second case the

geometry to be simulated does not include the tip itself. Thus, in case two only a cantilever beam, positioned at a respective distance including the tip height (Figure 24), is simulated. It has to be noted that the centre of rotation is the tip apex, also in case that the tip is not explicitly accounted for the electric field calculations.

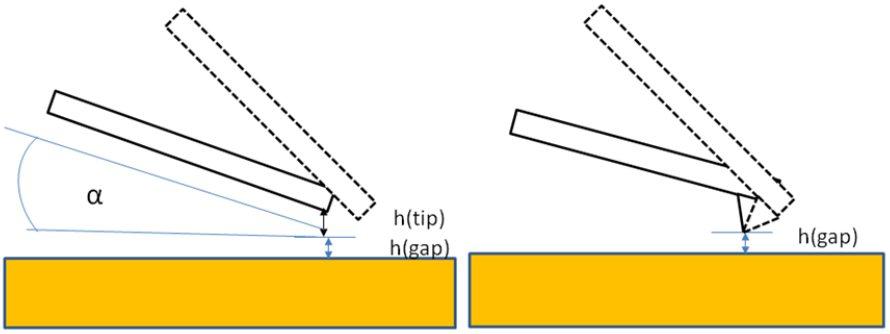

Figure 24. (left) cantilever model without tip (2D and 3D); (right) cantilever model including tip. Note, that the rotation centre is placed at the tip apex.

It was further investigated to reduce the task to a simplified two-dimensional problem without taking into account the cantilever's tip. Since the structure has a plane of symmetry, only half of the geometry was considered for the 3D case. The mirror symmetry was considered by the Comsol Multiphysics model.

The following assumptions were made in the models:

(i) The cantilever is made of Si, which was considered as a perfect conductor and thus the surface of the cantilever is perfectly grounded.

(ii) The bias voltage is applied at the sample (bottom of simulation area).

(iii) All other boundaries are electrically insulated.

(iv) Simulations considers only stationary solutions, dynamic effects are neglected.

(v) The cantilever is rigidly clamped at one end.

The models parameters are summarized in the Table II**.** Cantilever and tip dimensions were estimated from SEM pictures (Figure 25, *a*). Since we indented to obtain the stability range for the FE-SPL mode the geometrical parameters (tip height, cantilever angle and thickness) were widely varied in the FEM model. Figure 25, *b* shows the resulting 3D geometry of the cantilever (including tip) and surrounding air block.

Table II – Summary of the model parameters applied:

Parameter	**Symbol**	**Value**	**Units**
Length of the cantilever	*L*	350	µm
Width of the cantilever	*W*	125	µm
Thickness of the cantilever	*H*	9… 10	µm
Tip height	*h*	6… 9	µm
Tip half-angle	β	13	degrees
Bias voltage	*V*	25… 45	V

Tip height: 6 µm

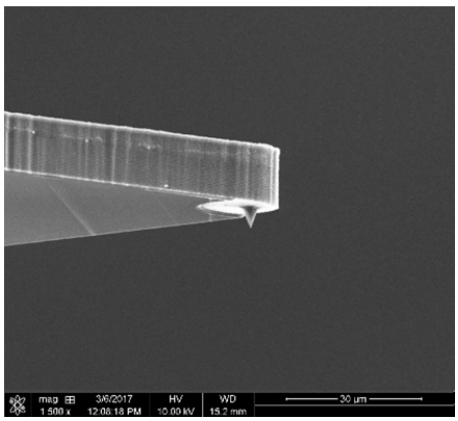

Tip height:9 µm

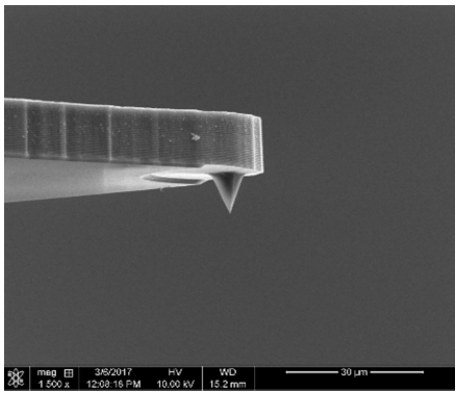

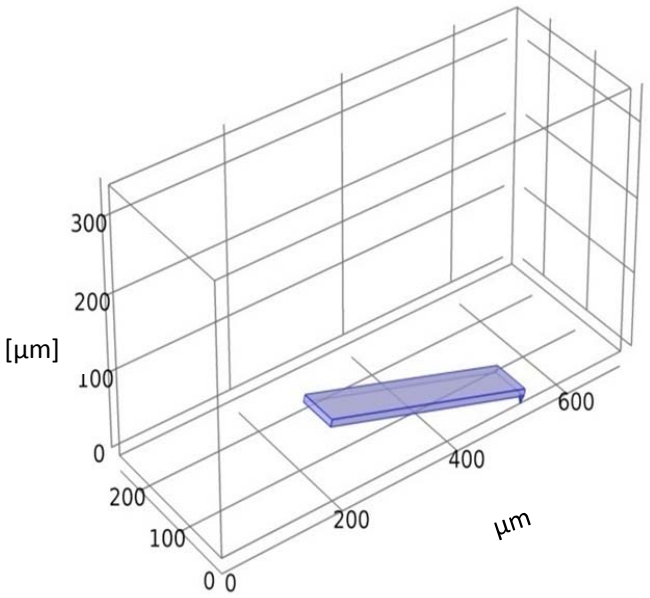

Figure 25. (a) SEM image of the cantilever applied for simulation and (b) its resulting 3D geometry implemented in the simulation.

On basis of grid-convergence tests the computational domain is discretized using approx. 900.000 tetrahedral elements for the 3D geometry (Figure 26, *a*) and 90.000 triangular elements in case of 2D. An example of the resulting 3D mesh near the tip is presented in Figure 26, *b*.

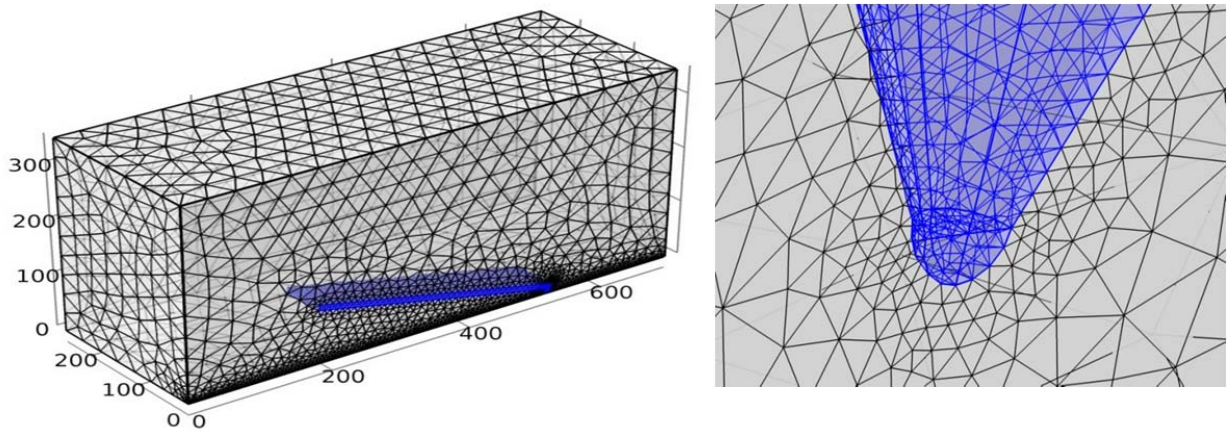

Figure 26. (a) 3D finite-element mesh; (b) fragment of the finite-element mesh near the tip.

The time needed to perform 3D calculation was about 234 minutes, while it took about 32 minutes to perform 2-D simulations.

d) SIMULATIONS RESULTS

Figure 27 shows an example of the electrostatic potential distribution obtained for an applied DC bias. The fringing areas can be clearly seen around the tip.

a)

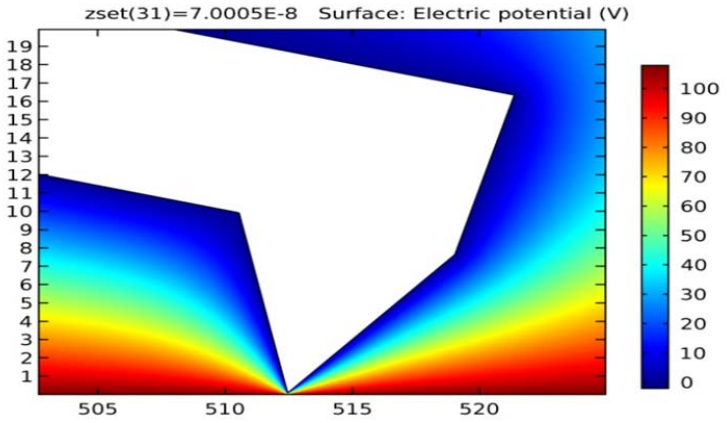

b)

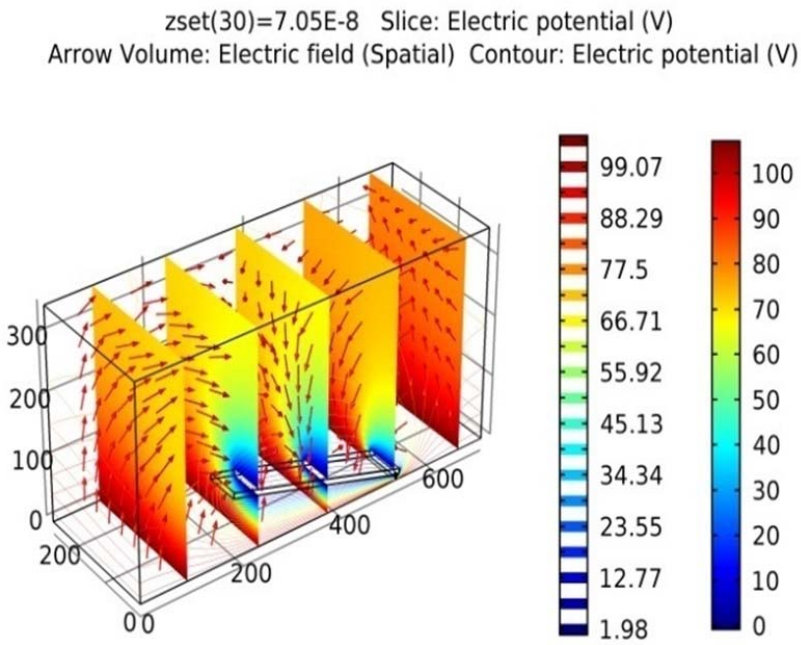

Figure 27. (a) Surface plot of the electrostatic potential near the tip. (b) 3D slice plot and iso-surfaces of the electrostatic potential and arrow plot of the electric field around the cantilever

In Figure 28-(a) the equilibrium displacement of the cantilever tip is shown in dependency of the applied voltage for different values of cantilever inclination angles. Results were obtained with the 2D model without tip, but rotation around the virtual top of the tip. Here, the initial gap d_{ts} was set to 100 nm.

However, due to the virtual tip the total gap between cantilever and sample is larger than the tip-sample distance d_{ts}, since it is increased by the tip height h. Due to this deflections larger than d_{ts} can be obtained (maximal deflection: $\leq d=h+d_{ts}$).

When a bias voltage is applied to the substrate the cantilever begins to bend towards the sample surface. For each voltage two deflection values are obtained. The smaller one belongs to the stable branch, whereas the larger one is the unstable one. The maximum voltage, where both deflection values are similar, corresponds to the pull-in voltage. As can be seen, in case of stiff cantilever (90 N/m) the pull-in voltage is quite high for the parameters used, i.e. 800 V for an angle of 45° and 1000 V for 15°. Deflection curves are not traced to the end in the unstable region because unstable branch is extremely difficult to capture due to convergence problems. An interesting effect is observed. The pull-in voltage is in case of 45° smaller than that for the 15° mounting, which is somewhat contradictory to the expectations that 15° should be more unstable than 45°. This deviation can be explained from the centre of rotation used in the simulations. Due to this, the effective distance between the front edges of the cantilever is smaller for 45° than for 15°. Thus, the electric fields for both realizations are quite different and the cantilever angle of 45° becomes unstable for smaller voltages than the 15°. Simulation results for soft cantilever are not shown here. As revealed and experimentally demonstrated, the effect occurs at significantly lower voltages of < 100 V.

In summary, the results indicate that the system operates at <100 V within the stable regime in case of stiff cantilever. However, in practice and under the combination of electrostatic and mechanical loads, other instabilities due to large bending and small gap, like a dynamic pull-in, could also occur at lower values of the bias voltage.

In Figure 28-(b) the region of interest for cantilever deflections between 0-100 nm is shown for different FEM models. It can be seen that the curves are quite similar. Only a small deviation of up to 10 V for a 100 nm deflection is obtainable. The quantitative differences between the curves observed with 3D and 2D geometries can be explained by the fringing fields near the tip and the sharp edges of the cantilever, which cannot be reproduced by the two-dimensional model. These fields have the effect of increasing the capacitance between tip and substrate and, consequently, the electrostatic force. Since the discrepancy in the typical range of voltage, tip-sample distance and deflections is small, further calculations were carried out using a 2D approach in order to save computing resources.

Next, the dependency of the cantilever bending as function of initial gap, stiffness of the cantilever, cantilever angle and the applied bias voltage was simulated. Therefore, a moving mesh technique was used to simulate the movement of the tip to the surface during the approaching process. For this purpose mesh displacement is assigned at the bottom boundary via a parametric sweep.

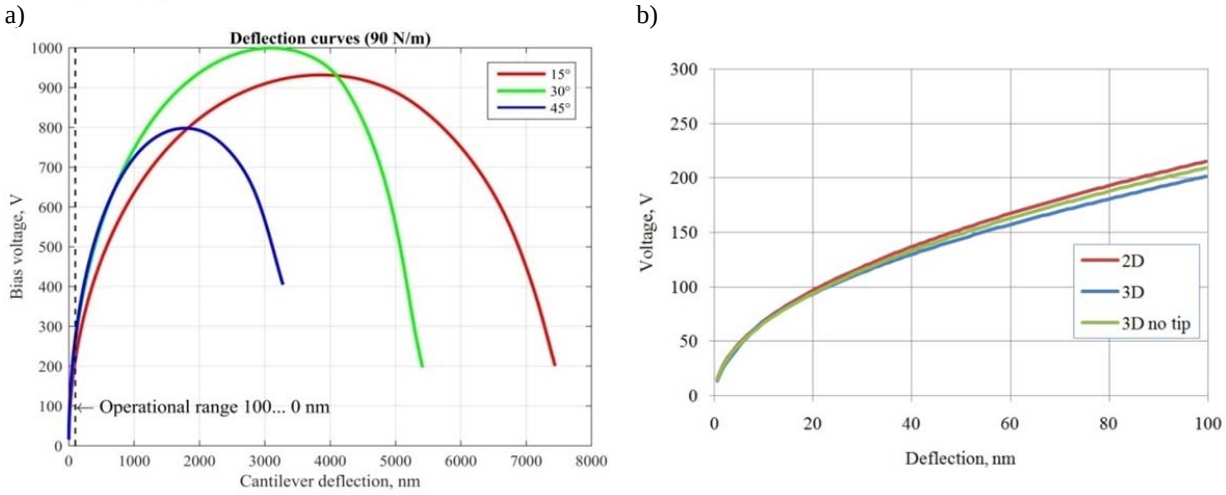

Figure 28. (a) The equilibrium relationship between cantilever deflection and voltage (the value of the initial gap in this simulations was set to 100 nm). (b) Enlarged image of the deflection in the range 0 - 100 nm (α = 15º).

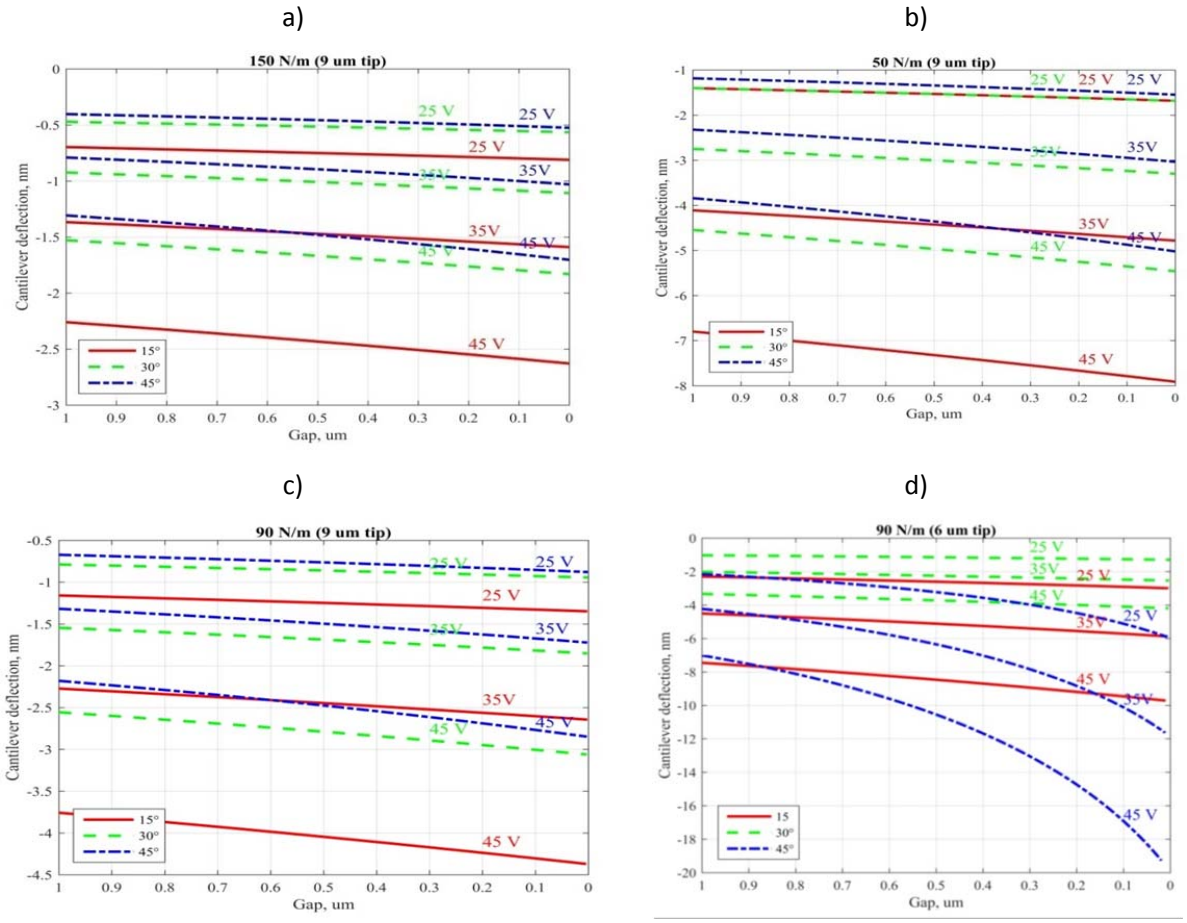

Figure 29. Quasi-static deflection-displacement curves for combination of spring constant and tip height (a) 50 N/m, 9 µm; (b) 90 N/m, 9 µm; (c) 150 N/m, 9 µm; (d) 90 N/m, 6 µm.

Summarized in Figure 29, the bias voltage was set to 25 V, 35 V and 45 V respectively, three different inclination angles 15° (red), 30° (green) and 45° (blue) were applied. An initial gap of 1 μm was used. The stiffness of the cantilever is changed by modification of the cantilever thickness. The corresponding spring constant of the cantilever is given above the graph.

As expected, the deflection increases with decreasing initial gap [see Figure 29 (a)] and increasing voltage due to enlargement of the electrostatic force. Thereby, a thicker cantilever (higher stiffness = 150 N/m, Figure 29 (a)] exhibits a smaller deflection and a smaller increase in deflection with decreasing deflection compared to a thinner (=softer) cantilever [Figure 29 (b)]. Moreover, as expected, with decreasing tip height the electrostatic force is increased, as can be seen from the comparison of Figure 29 (c) (9 µm tip height) and (d) (6 µm tip height).

In case of large tip heights (9 µm) the dependency of the inclination angle is as expected, i.e. the smaller the inclination angle the larger the deflection, Figure 29 (c). Surprisingly, with changing cantilever angle the dependence of the deflection on the initial gap is altered. While a linear dependence is observed for 15° and 30° in the considered operation range, a nonlinear behaviour is seen for 45°. This is even more pronounced in case of smaller tip heights, e.g. 6 µm Figure 29 (d). Due to this nonlinearity, for the small tip the 45° angle results in the largest deflection. This nonlinear behaviour can be caused on one hand by the rotation centre, which results in an effectively smaller gap between cantilever and sample, and on the other hand by the fringing electric field, which is pronounced for larger inclination angles.

(e) Summary

The modelling of the FE-SPL cantilever leads to a set of coupled nonlinear boundary value problems and a set of coupled nonlinear equations, respectively. These coupled nonlinear systems were solved numerically and the pull-in parameters of single cantilevers were obtained.

In the case of stiff cantilever (≈90 N/m) the pull-in voltage is significantly larger than the typical operation voltages. Furthermore, for very small gaps the influence of Casimir and van-der-Waals forces cannot be neglected. These should be important in the range of large emission currents. Thus, the interactions between the electrostatic force and the mechanical properties of the cantilever should be further investigated. The comparison of the 2D and 3D model, with and without tip, reveal that in the model of the electrostatic force the fringing electric field effect has to be taken into account. It results in a reduction of the stable operating regime.

8. Demonstration of parallel field emission scanning probe lithography (FE-SPL) capability using Quattro cantilever arrays:

As reported before, due to the trade-off problem (cantilever stiffness vs. available actuation range of individual cantilever) we were only able to demonstrate parallel field emission scanning probe lithography with two neighbouring cantilever of a "Quattro" cantilever array. Here, 9 nm resist films are prepared by spin-coating on top of pre-structured SOI chips (SNM chips). In order to minimize the parasitic electrostatic actuation effect (as described in section 7) when applying a sample bias voltage stiff cantilevers were applied, characterized by k_{nom} of 90 N/m. Further, cantilever arrays with highest tips were applied, in particular 9 µm. The cantilever has typical tip radii of approx. 30 nm. The preliminary results are shown in Figure 30, 31, 32 and 33, whereas Figure 30 and 31 are taken before and Figure 32 and 33 after pattern transfer by cryogenic plasma etching.

In Figure 30 SEM image the simultaneous patterning of two adjacent meander lines in positive tone (= direct, development-less removal of resist) by two active cantilever is visible. A vector-based line patterning routine was applied. A sample bias voltage of +46 V (writing tips are individually grounded through IV-preamplifier) and a current set-point of 28 pA for each cantilever was applied. A tip velocity of 1 µm/s was applied. As revealed by Figure 30 both patterns written by two neighbouring cantilever of an array are identical. However, the current regulation was lost at the end of each meander line, which could be attributed to the remaining sample tilt and the limited actuation range of each cantilever (DC actuation operated at the limit).

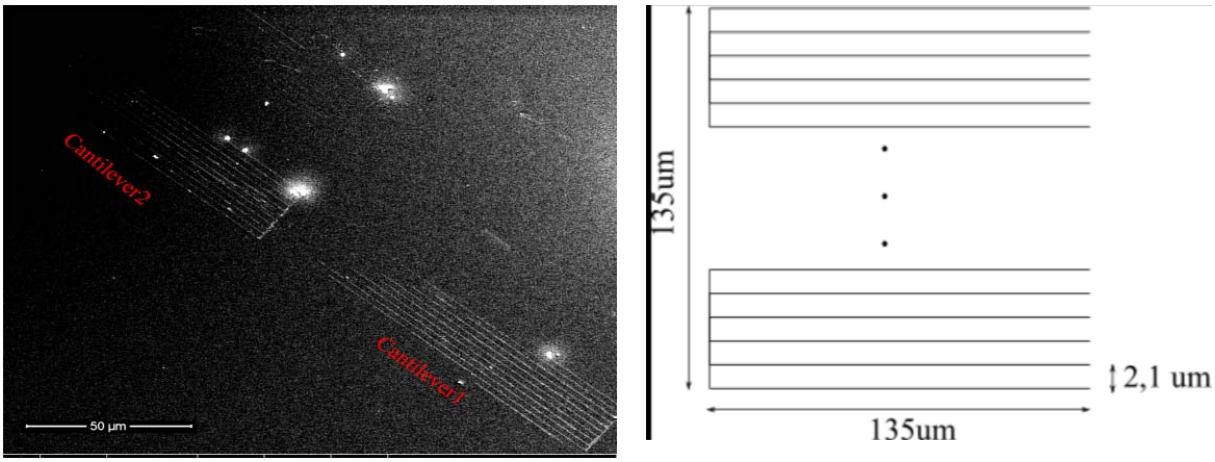

Figure 30. SEM image of meander lines patterned simultaneously with two cantilever of a "Quattro" cantilever array. The first patterning was successful, whereas the second patterning approach (see upper part of the image) was unsuccessful. The crash point of the second cantilever is visible.

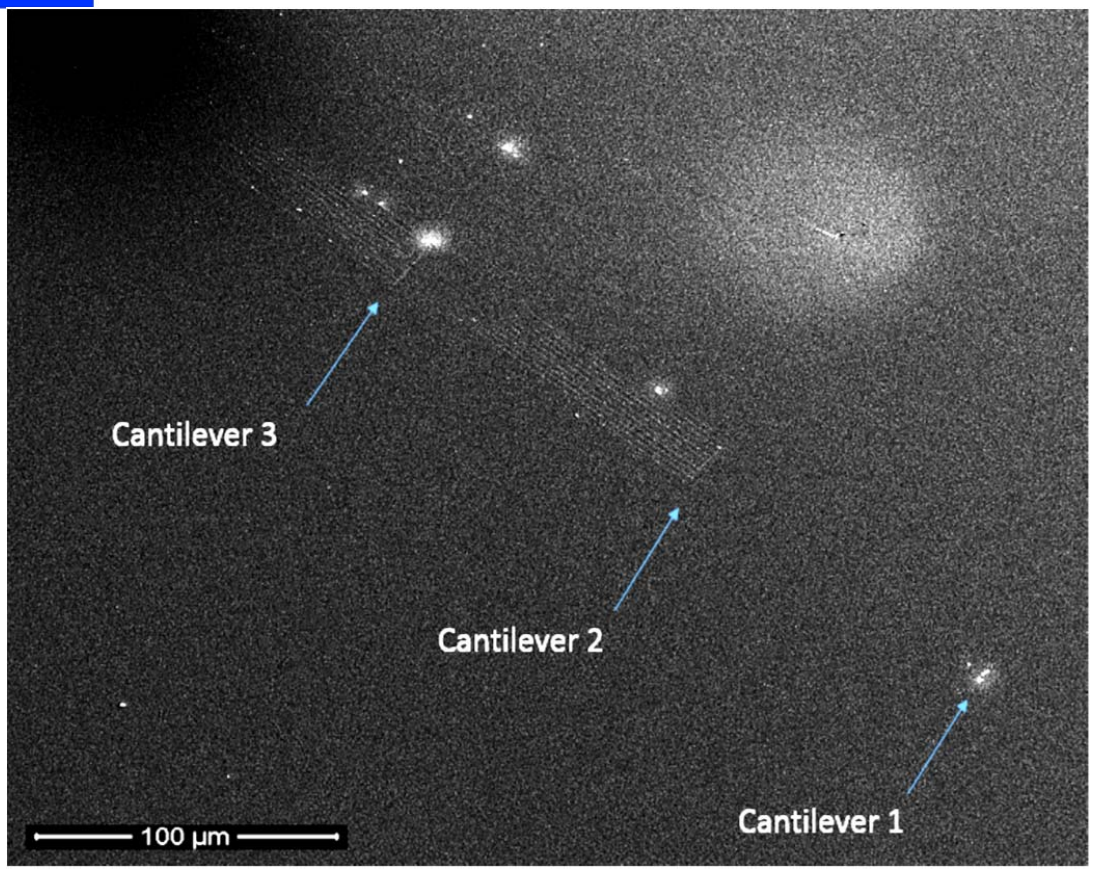

Figure 31. SEM image of a lithographic result achieved by using a "Quattro" cantilever array. Simultaneous FE-SPL with 3 cantilever out of 4 were performed.

In Figure 31 the same FE-SPL test as in Figure 30 is shown, whereas additionally the interaction induced by the first cantilever is visible. Here, cantilever 1 crashed several times and probably lost the tip. This is caused by the inappropriate DC actuation range, which is well below the required range in order to compensate the tip-sample spacing offset in an array. Thus, the cantilever is approached to close to the surface, whereas the actuation was not able to regulate.

After lithography the simultaneously patterned lines are etched into the underlying Si by a cryogenic plasma etching process (ref. D1.3; -120°C, 45 sec). Afterwards, the features are measured by SEM and AFM shown in Figure 32 and 33, respectively. The line width measured by AFM was approx. 100 nm. In summary, we have demonstrated the general parallel operation capability of FE-SPL using "Quattro" cantilever arrays. However, further technical issues, as described before, has to be solved in order to demonstrate an applicable parallel cantilever lithography.

a)

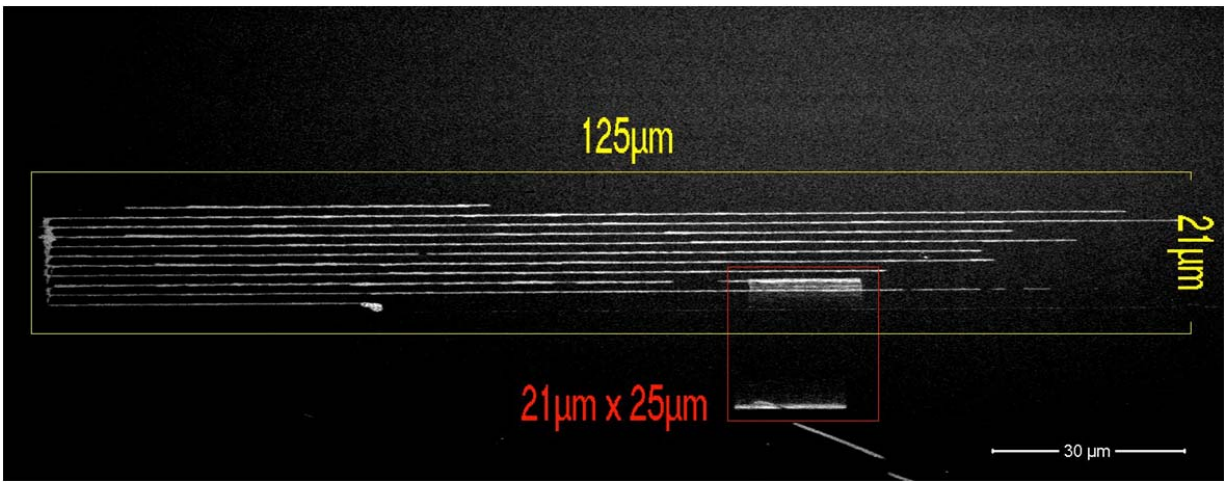

b)

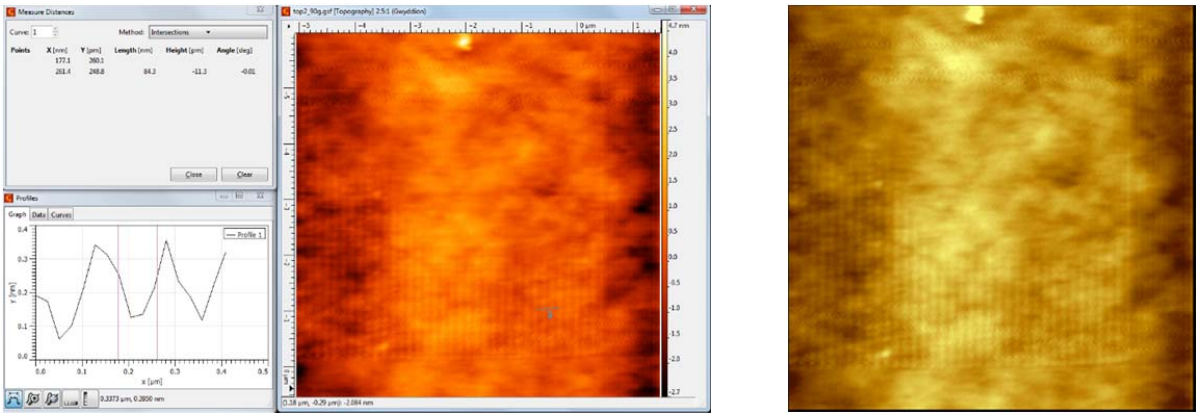

Figure 32. (a) SEM image of FE-SPL features written with a single cantilever from the "Quattro" array. The patterns are transferred into the underlying Si by a cryogenic plasma etching process. There are two overlapped fields: (yellow) 125 µm x 21 µm; and (red) 21 µm x25 µm; (b) Corresponding AFM image of 21 µm x 25 µm patterning field, marked in (a) with a red rectangle.

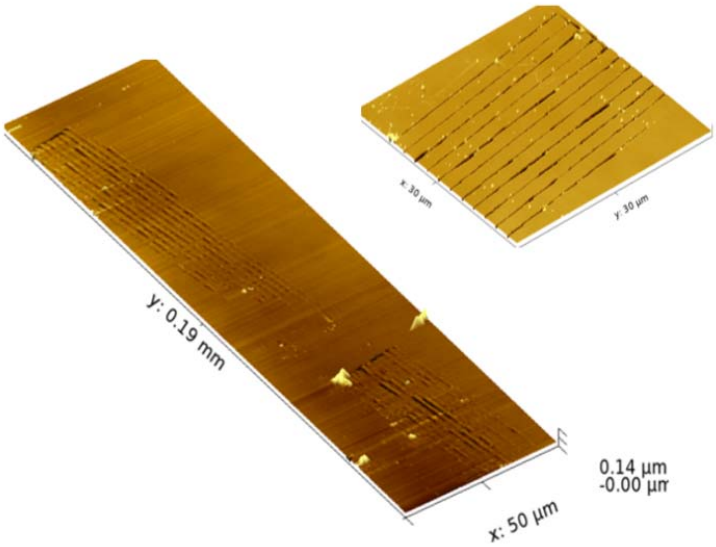

Figure 33. AFM images corresponding to Figure 30, taken after pattern transfer. In contrast to writing with a single cantilever, keeping all cantilever on equidistance to the surface was very difficult to achieve. As a result, tip "crashes" and "scratching" of the tip over the resist surface is likely to be caused.